Connecting the Dots for Fundamental Understanding of Structure-Photophysics-Property Relationships of COFs, MOFs, and Perovskites using a Multiparticle Holstein Formalism

Raja Ghosh*,† and Francesco Paesani*,†,‡,¶

†*Department of Chemistry and Biochemistry, University of California San Diego,*
La Jolla, California 92093, United States
‡*Materials Science and Engineering, University of California San Diego,*
La Jolla, California 92093, United States
¶*San Diego Supercomputer Center, University of California San Diego,*
La Jolla, California 92093, United States

E-mail: raghosh@ucsd.edu; fpaesani@ucsd.edu

Abstract

Photoactive organic and hybrid organic-inorganic materials, such as conjugated polymers, covalent organic frameworks (COFs), metal-organic frameworks (MOFs), and layered perovskites, display intriguing photophysical signatures upon interaction with light. Elucidating structure-photophysics-property relationships across a broad range of functional materials is nontrivial and requires our fundamental understanding of the intricate interplay among excitons (electron-hole pair), polarons (charges), bipolarons, phonons (vibrations), inter-layer stacking interactions, and different forms of structural and conformational defects. In parallel with electronic structure modeling and data-driven science that are actively pursued to successfully accelerate materials discovery, an accurate, computationally inexpensive, and physically-motivated theoretical model, which consistently makes quantitative connections with conceptually complicated experimental observations, is equally important. Within this context, the first part of this Perspective highlights a unified theoretical framework in which the electronic coupling as well as the local coupling between the electronic and nuclear degrees of freedom can be efficiently described for a wide range of quasiparticles with similarly structured Holstein-style Hamiltonians. The second part of this Perspective discusses excitonic and polaronic photophysical signatures in polymers, COFs, MOFs, and perovskites, and makes a unique attempt to bridge the gap between different research fields using a common theoretical construct - the Multiparticle Holstein Formalism. We envision that the synergistic integration of state-of-the-art computational approaches with the Multiparticle Holstein Formalism will help identify and establish new, transformative design strategies that will guide the synthesis and characterization of next-generation energy materials optimized for a broad range of optoelectronic, spintronic, and photonic applications.

Introduction

A fundamental understanding of excited-state phenomena and the elementary mechanisms that govern photophysical and charge transport processes of multifunctional materials is crucial for new scientific breakthroughs and future technological innovations. Fueled by the discovery of polymer-based light emitting diodes (OLEDs),[1,2] organic materials continue to find increasing commercial value, with a broad range of applications in photovoltaics,[3–8] organic spintronics,[9–12] field effect transistors,[13–16] wearable technology,[16–19] flexible displays,[20–23] photolithography,[24,25] and chemosensors and bioprobes.[4,26,27]

In addition to traditional one-dimensional semiconducting polymers, the discovery of 2D covalent organic frameworks (COFs) in 2005[28] has sparked renewed interest in organic electronics. COFs represent an emerging class of porous organic materials that offer a range of unique advantages compared to traditional polymeric materials, such as morphological precision and positional control of diverse functional building blocks.[28–45] Tremendous efforts are currently focused on taking advantage of the structural diversity, crystallinity, and porosity of various COF structures for potential cutting-edge applications in biomedicine and bioimaging,[46–50] drug and gene delivery,[51–54] gas and energy storage,[55–58] photocatalysis,[59,60] and ion conduction.[61,62] Despite the presence of intrinsic porosity, which hinders the efficient movement of charges, COFs have also found applications as semiconducting materials.[63–72] Energy and charge migration in COFs happen through the efficient transport of excitons and polarons, respectively, either along the framework backbone (i.e., through bond) or between the π-stacked layers (i.e., through space).

While the facile synthesis of organic materials makes optoelectronic devices inexpensive compared to their inorganic counterparts, structural and conformational disorder often leads to poor conductivity and low mobility.[73–77] Despite being environmental friendly, organic thermoelectric materials also suffer from low conductivity, Seebeck coefficient, and power factor.[78] The flexibility of self-assembling organic and inorganic building units to form hybrid organic-inorganic frameworks offers the possibility to combine unique photophysical and electronic properties that are absent in either of the individual building blocks.[78–80] Combining the high conductivity of the inorganic component with stronger light-matter interactions and higher quantum efficiency of the organic components was proven to be an effective approach which resulted in much improved electrical, optical, and transport properties.[80–84] Over the last decade, hybrid organic-inorganic materials, such as metal-organic frameworks (MOFs) and layered perovskites, have received widespread interest for potential applications in various fields of chemistry and materials science.[85–93] Although MOFs are generally considered as insulating materials, recent studies have reported promising results on the synthesis of intrinsically conducting MOFs.[94–97] The field of layered perovskites has exploded in the last decade, and two-dimensional (2D) perovskites have emerged as promising candidates for next generation solar cells owing to record power conversion efficiencies which vastly outperform the efficiencies achieved by organic based materials.[98–102]

The design and synthesis of new materials presents a formidable challenge since chemical manipulation and framework diversity, in principle, allow for myriads of possible structural combinations that enable the fine tuning of optical, electronic, and transport properties. From an experimental viewpoint, establishing efficient synthetic routes for synthesizing novel electronic materials tailored for specific applications remains the main obstacle.

To overcome some of the challenges, computational predictions of new multifunctional materials has been bolstered primarily due to the development of new algorithms and the availability of supercomputers which readily enable the treatment of large number of molecules within a reasonable time frame. Various computational and theoretical approaches, ranging from Quantum Monte Carlo (QMC) to molecular dynamics (MD) simulations and Density Functional Theory (DFT) have been utilized to gain new insights into the complicated electronic structure of organic and hybrid materials.[103] For example, DFT in combination with tight-binding modeling has been extensively employed to investigate the nature of flat bands,[104] electronic structure,[105,106] structural defects,[107] effects of doping,[108] and interlayer stacking interactions[109] in 2D COFs.

Skillful exploration of data through data-mining and big data approaches as well as electronic structure modeling have greatly benefited the fields of MOFs and perovskites.[103,110–119] Machine learning and high throughput techniques have been routinely employed to screen the chemical space of hybrid materials with the goal of proposing new MOF and perovskite structures that are suitable for different applications, including but not limited to catalysis,[120–123] gas storage and separation,[124] and optoelectronics.[125–128] While materials modeling based on data-driven approaches has achieved some remarkable success in predicting electronic properties (e.g., band gaps, charge densities, electronic couplings, oscillator strengths, etc.), the development of a rigorous theoretical framework that can use the calculated properties to make direct and quantitative connections with state-of-the-art experimental observations will further help accelerate materials discovery.

Within this context, the majority of optoelectronic, charge transport and storage, and photonics applications involve the fundamental photophysical process of absorption and emission of light. Excited state processes of technologically relevant organic and hybrid materials such as polymers, COFs, MOFs, and perovskites are mainly governed by the quantum mechanical behavior of mobile quasiparticles, such as Frenkel, charge-transfer, and Wannier-Mott excitons, polarons and bipolarons, trions, and the interaction of these quasiparticles with intra- and inter-molecular vibrational modes.[129–144] These vibronic effects, which arise from the coupling of electronic transitions with the nuclear vibrational motion, play a central role in determining the photophysical response of organic[145,145–147] and hybrid materials[148–154] as well as excited state dynamics in chemical and biological systems.[155–161,161–163] It is therefore not surprising that any progress in the design of novel materials warrants a robust theoretical methodology that can provide an in-depth understanding of how the complicated interplay between photons, excitons, polarons, bipolarons, phonons, and spins influences the photoinduced excited state processes of a wide range of materials.

Despite significant recent progress, two main challenges still persist which involve a quantitative understanding of how electron-phonon coupling and defects influence the electronic, optical, and transport properties of functional electronic materials. Although, excited state properties of materials can be modeled using linear-response time-dependent density functional theory (LR-TDDFT) or the Bethe–Salpeter equation (BSE),[164] the presence of a large number of atoms in 2D materials makes the application of LR-TDDF and BSE computationally very demanding (however, recent advances look very promising[165,166]). Moreover, electron-phonon coupling and different forms of electronic and conformational defects play fundamental roles in determining the photophysical response and, consequently, the transport properties of most organic and hybrid materials. Although, LR-TDDFT/BSE approaches have been successfully employed to investigate the photophysical response of MOFs,[167–171] COFs,[141,172–174] and perovskites,[130,142,175–182] to the best of our knowledge, none of the existing methodologies simultaneously take into account aggregation, electronic coupling, strong electron-phonon coupling, and crystalline disorder on equal footing.

An exact treatment of electron-phonon coupling is a pressing challenge since the Hilbert space for most quantum systems grows exponentially with increasing system size and number of molecules. Overcoming this computational complexity involves the inevitable approximation of sacrificing the quantum description of the nuclei, which reduces to treating the nuclear motion adiabatically by employing the Born-Oppenheimer approximation (BOA). First-principles calculations based on the BOA such as finite differences and density functional perturbation theory have been used to interpret optical properties, charge transport, and defects in semiconductors.[183] However, this perspective highlights photophysical processes in which the nuclear vibrational kinetic energies are not negligible and undergo rapid nuclear reorganization, which therefore necessitates the explicit inclusion of nuclear quantum effects and, consequently, invalidates the BOA. In this regard, it should be noted that excellent non-adiabatic approaches, including mixed quantum-classical descriptions, have been successfully employed to investigate the photophysical processes and excited state dynamics of various systems.[184–189]

Coarse-graining is another efficient strategy to quantitatively describe electron-phonon coupling in large, non-rigid "vibronic" systems. Since the pioneering work by Drude,[190,191] Sommerfield,,[192] Hubbard,[193] Heisenberg,[194] Holstein[195,196] among others, coarse-grained tight-binding model Hamiltonians have been successfully employed to investigate the electronic, optical, and transport properties of materials.[104–106,197–201] The major approximation typically employed in tight-binding modeling involves simplifying the complicated many-body electronic system to an one-electron or single orbital model. In Holstein-based approaches, another major simplification is the harmonic oscillator approximation which considers the nuclear displacements as coupled quantum harmonic oscillators. Such simplifications are however not sufficient for practical applications, since the exact diagonalization becomes computationally intractable for large "vibronic" systems, which is the focus of this perspective. For example, the Holstein model can be exactly solved only for a few sites. Besides various approaches proposed in the literature to address this problem, including hierarchial equations of motion,[202–205] one potential solution is to specifically choose an accurate basis set for the diagonalization of the Holstein Hamiltonian. In this context, the multiparticle basis set, pioneered by Philpott,[206] developed and glorified by Spano,[146,147,207–209] and employed by others[210–215] has proved to be an excellent choice for diagonalizing the Holstein Hamiltonian. Multiparticle modeling of the Holstein Hamiltonian quickly becomes computationally expensive with increasing dimensions of the material unit cell, which is particularly relevant in the case of porous frameworks such as COFs and MOFs. In this context, taking advantage of sparse matrix techniques and MPI parallelization on multinode clusters, we have shown that it is possible to extend the application of multiparticle modeling to large "vibronic" 3D systems, with no loss of accuracy.[216,217]

The theoretical model, henceforth referred to as the Multiparticle Holstein Formalism (MHF), is based on a coarse-grained Holstein-style Hamiltonian in which electronic coupling, electron-phonon coupling, electrostatic interactions, and different forms of long- and short-range defects are treated on equal footing without invoking the BOA. The key advantage of the MHF is the nonadiabatic treatment of the electron-phonon coupling which allows for a fully quantum-mechanical treatment of both the kinetic and potential energies of the nuclei, thus bypassing the BOA. As described in Section 2, the MHF enables a unified and robust formulation that successfully describes vibronically dressed quasiparticles in molecules and materials. The MHF has been very successful in accounting for the spectral properties of molecular aggregates and crystals,[145,147,207,210,211,218,219] conjugated polymers,[220–232] COFs,[216,217] and layered perovskites,[233] both in the mid-infrared (MIR) and UV-vis spectral regions. The ability to perform quantum calculations at the cost of classical simulations opens the door to MHF modeling of a wide range of 2D electronic materials for future advancements.

The article is organized as follows: In Section 2 we briefly discuss the MHF and show that the electronic coupling as well as the local coupling between electronic and nuclear degrees of freedom for various quasiparticles can be efficiently described with similarly structured Holstein-style Hamiltonians that can be diagonalized using a multiparticle basis set. Section 3 highlights the photophysical signatures of Frenkel, charge-transfer, and Wannier-Mott excitons in organic (polymers and COFs) and hybrid (MOFs and perovskites) materials. The role of "excitonic polarons", i.e., excitons dressed with intramolecular vibrations is also discussed. Special emphasis is placed on understanding how several factors, such as the nature of aggregation, packing arrangement, particle size, relative humidity, and defects determine the UV-vis to near-IR spectral response of donor-acceptor (D-A) COFs. The exciton fine structure observed in layered perovskites, which is a topic of considerable speculation,[152,234–236] is also discussed. Section 4 focuses on the MIR photophysical response of polarons and the correlations between MIR signatures and polaron coherence lengths. The similarity in the spectral response of polarons in polymers, COFs, MOFs, and perovksites is highlighted, and some of the factors affecting charge transport are reviewed. It is a daunting task to provide a comprehensive review that includes all relevant references on photophysical processes observed in organic and hybrid materials and this perspective only focuses on select photophysical signatures that are intriguing from the point of view of the MHF. Although previous reviews and perspectives have separately focused on optoelectronic processes in organic and hybrid materials,[144,237–242] to the best of our knowledge, no prior studies have attempted to provide an interpretation of the photophysical signatures of both organic and hybrid materials using a common theoretical platform - the MHF.

Theoretical Framework

Upon electronic excitation, local electron-phonon coupling is associated with significant nuclear relaxation along one or more intramolecular vibrational coordinates. The creation of neutral excitations (e.g., excitons) or charged excitations (e.g., polarons) in conjugated organic molecules,

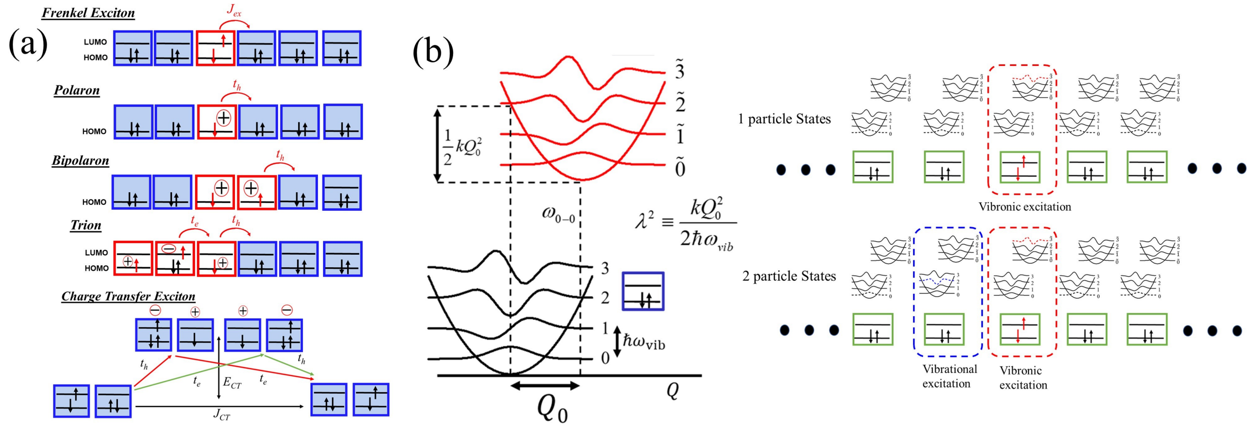

Figure 1: (a) Simplified view of various forms of neutral and charged excitations. (b) Nuclear potential well corresponding to the aromatic to quinoidal stretching mode, Q, in the ground and excited electronic states for each isolated molecular unit. ω_{vib} refers to the vibrational energy and the nuclear relaxation energy is denoted by $\lambda^2\omega_{vib}$.(c) Schematic showing one-particle states, i.e., vibronic excitations (top panel) and two particle states, i.e., vibronic/vibrational exciton pair.

which is present in MOFs, COFs, and perovskites, is accompanied by significant nuclear relaxation, the bulk of which occurs along the aromatic to quinoidal stretching vibrational mode having a frequency that lies in the range between 0.16 eV-0.18 eV.[147,207,219] This local nuclear relaxation energy plays a central role in the photophysical and transport properties, examples of which will be discussed later in the context of COFs, MOFs, and perovskites. In what follows, in our coarse-grained approach, a simple schematic of a linear assembly of coupled chromophores (or units) that can host various types of neutral and charged excitations is shown in Fig. 1a.

Frenkel Exciton

In the subspace containing a local Frenkel excitation (see Fig. 1a), where the n^{th} repeat unit in the lattice denoted by $|n\rangle$ hosts an electron-hole pair (i.e., a Frenkel exciton), the Hamiltonian (with $\hbar$ = 1) can be divided into electronic and vibronic contributions,

$$H_{FE} = H_{FE-el} + H_{FE-vib} \tag{1}$$

with the purely electronic part of the Hamiltonian given by

$$H_{FE-el} = \omega_{0-0} \sum_{n} |n\rangle\langle n| + \sum_{m,n} J_{m,n} \{ |m\rangle\langle n| + |n\rangle\langle m| \} \tag{2}$$

and the vibrational energies and vibronic coupling are given by

$$H_{FE-vib} = \omega_{vib} \sum_{n} b_n^{+} b_n + \lambda \omega_{vib} \sum_{n} (b_n^{+} + b_n + \lambda) |n\rangle\langle n| \tag{3}$$

In Eq. 2, the first term represents the energy of the Frenkel exciton. Exciton transport between neighboring sites $|n\rangle$ and $|m\rangle$ is governed by long-range intermolecular Coulomb coupling as well as a short-range superexchange contribution which mainly arises due to wavefunction overlap between the adjacent chromophores. The coupling values are generally derived from atomic transition charge densities and can be calculated using TDDFT methods.[243–246] Upon electronic excitation, Frenkel excitons in π-conjugated organic molecules couple very strongly to the aromatic to quinoidal vibrational mode, ω_{vib}, with frequency in the range between 1200-1500 cm^{-1}. The two terms in Eq. 3 account for the vibronic coupling where the operators b_n^{+} (b_n) create (annihilate) a vibrational quantum of energy on the n^{th} unit in the ground state (S_0) of the corresponding potential energy well. The strength of the electron-phonon coupling is governed by the Huang-Rhys (HR) factor, λ^2, and the nuclear relaxation energy upon vertical Franck-Condon excitation is given by $\lambda^2\omega_{vib}$. λ^2 is a dimensioless quantity that determines the relative displacement of the minima of the ground and excited potential well along the intramolecular vibrational coordinate. In the case of excitons in conjugated polymers, the value of λ^2 generally lies between 1 and 2.[231]

Charge-Transfer Exciton

In closely packed structures, such as polymers, COFs, and MOFs, where the inter-chain/inter-framework π-stacking distances generally lie in the range between 0.30 nm and 0.40 nm, there exists significant π-orbital overlap between the HOMO and LUMO of neighboring π-conjugated units. In these scenarios, local Frenkel excitations dissociate into charge-transfer states, with the electrons and the holes residing on neighboring units, as shown in Fig. 1a. As a consequence, considering only long-range intermolecular Coulomb coupling is not sufficient to accurately describe the underlying physics of the system, and short-range superexchange contributions arising from wavefunction overlap need to be considered. Similar to Frenkel exciton, the appropriate vibronically-coupled charge-transfer Hamiltonian (with $\hbar = 1$) can be similarly divided into electronic and vibronic contributions,

$$H_{CT} = H_{CT-el} + H_{CT-vib} \tag{4}$$

with the purely electronic part given by

$$\begin{aligned} H_{CT-el} &= \sum_n \sum_{s=-1,1} \{t^e_{n,n+s}|n\rangle\langle n,n+s| + h.c.\} \\ &+ \sum_n \sum_{s=-1,1} (t^h_{n,n+s}|n\rangle\langle n+s,n| + h.c.\} \\ &+ \sum_n \sum_{s=-1,1} E^{CT}_{n,n+s}|n,n+s\rangle\langle n,n+s| \end{aligned} \tag{5}$$

and the vibrational contribution given by

$$\begin{aligned} H_{CT-vib} &= \omega_{vib} \sum_{n,s=-1,1} \{\lambda_+(b_n^+ + b_n + \lambda_+) \\ &+ \lambda_-(b_{n+s}^+ + b_{n+s} + \lambda_-)\}|n,n+s\rangle\langle n,n+s| \end{aligned} \tag{6}$$

where the charge-transfer excitations are limited to nearest neighbors. The charge-separated state is denoted by $|n,n+s\rangle$, with sites $|n\rangle$ and $|n+s\rangle$ hosting a cation and an anion, respectively. In Eq.5, the first two terms account for nearest-neighbor hopping of the electron and the hole, respectively, and E_{CT} defines the energy of the charge-separated state. In addition to the ground-state nuclear potential, there exist three excited-state nuclear potentials corresponding to the fragment's electronic states representing a Frenkel-like excitation, a cation, and an anion, respectively. As shown in Fig. 1b, all potentials are assumed to have identical curvature but are generally shifted relative to the ground state potential based on the value of HR factors. For Frenkel-like excitations, the HR factor is defined as λ^2, while the HR factors for the cations and anions are λ_+^2 and λ_-^2, respectively, as shown in Eq. 6. $\lambda_+^2 \omega_{vib}$ and $\lambda_-^2 \omega_{vib}$ determine the cationic and anionic nuclear relaxation energies respectively. Both vibronic coupling and charge-transfer mediated interactions strongly influence the photophysical and transport properties of the organic molecules, which are the primary building blocks of COFs and are also present in hybrid materials as discussed in Sections 3 and 4.

Polaron

Analogous to the case in Frenkel excitons, Eq. 1 can also be efficiently used to describe polarons. Unlike in the case of excitons, where the n^{th} unit in Eq. 2 denotes an electron-hole pair, the n^{th} unit in Eq. 2 for polarons indicates a charge as shown in Fig. 1a. In addition, differently from excitons, in the case of polarons, charge transport between sites $|n\rangle$ and $|m\rangle$ is mainly governed by the charge resonance integral, $t_{m,n}$, which can be evaluated by electronic structure methods.[247,248] Finally, while the exciton model retains the local HOMO and LUMO for each site $|n\rangle$, only the local HOMO for each repeat unit, $|n\rangle$, is retained in the case of polarons, as shown in Fig. 1a. For both excitons and polarons, the first term in Eq. 2 determines the energy of the excited state of the isolated unit which hosts the exciton/polaron relative to the ground state which contains no excitons or polarons. In the case of excitons, ω_{0-0} in Eq. 2 refers to the adiabatic energy required to create an electron-hole, while in the case of polarons, ω_{0-0} refers to the ionization energy required to create the hole. However, just like in the exciton model, creation of polarons is also accompanied by significant nuclear relaxation along the dominant aromatic-quinoidal stretching coordinate. The value of λ^2 in the case of polarons is approximately half of the exciton value.[249]

Bipolaron

The basis set expressing the Hamiltonian in Eq. 1 consisted of single excitons or single polarons. The Hamiltonian in Eq. 1 can be readily extended to include two excitations, i.e., bipolarons which would need additional terms such as electrostatic Coulomb repulsion between the two polarons. Neglecting the contribution from the spin component, the Hamiltonian for bipolarons can be similarly divided into electronic and vibronic components as[250]

$$H_{BP} = H_{BP-el} + H_{BP-vib} \tag{7}$$

Here, the electronic part of the bipolaron Hamiltonian in the subspace containing two holes is given by

$$\begin{aligned} H_{BP-el} &= t_h \sum_{\substack{m,n \\ (n>m)}}{}' \{|m,n\rangle \langle m,n+1| + |m,n\rangle \langle m+1,n| + h.c.\} \\ &+ \sqrt{2} t_h \sum_{m} \{|m,m\rangle \langle m,m+1| + |m,m\rangle \langle m-1,m| + h.c.\} \\ &+ \sum_{\substack{m,n \\ (n\geq m)}} V_{m,n} |m,n\rangle \langle m,n| \end{aligned} \tag{8}$$

where the first term takes into account the hopping of the polarons, which remain separated on distinct sites (indicated by the prime), and the second term accounts for the transport of the hole when both the holes occupy the same site in the lattice. The last term in Eq. 8 considers the electrostatic Coulomb repulsion between the two holes. To account for coupling of both the holes to the aromatic-to-quinoidal vibrational mode, the vibronic contribution of the Hamiltonian (with $\hbar = 1$) is given by

$$\begin{aligned} H_{BP-vib} &= \omega_{vib} \sum_{n} b_n^+ b_n \\ &+ \omega_{vib} \lambda \sum_{\substack{m,n \\ n>m}} \{(b_n^+ + b_n + \lambda) + (b_m^+ + b_m + \lambda)\} |m,n\rangle \langle m,n| \\ &+ \omega_{vib} \lambda \sum_{n} \{(b_n^+ + b_n + \lambda)\} |n,n\rangle \langle n,n| \end{aligned} \tag{9}$$

The Hamiltonian in Eq. 9 can be similarly extended to treat biexcitons, which have important applications in nonlinear optics.

Multiparticle Basis Set

A multiparticle basis set, pioneered by Philpott,[206] can be used to efficiently describe quasiparticles using Holstein-style Hamiltonians. In the multiparticle basis set, each basis function contains information about the location of the vibronically excited chromophore as well as additional purely vibrationally excited molecules.

A single-particle basis state which can either be a single hole or a single exciton as shown in Fig. 1a is denoted as $|n,\tilde{v}\rangle$ to indicate that the hole or the exciton resides on the n^{th} unit with $\tilde{v}$ vibrational quanta in the shifted (S_+) potential well (Fig. 1c). All the remaining units are in their vibrationless ground states, which implies that the units have filled HOMOs with no vibrations in the S_0 well. In a two-particle basis state, denoted as $|n,\tilde{v};n'v'\rangle$, the n^{th} unit is ionized with $\tilde{v}$ vibrational quanta in the S_+ potential well, while the unit at n' is electronically neutral, with $v' > 0$ vibrational quanta in the unshifted S_0 potential well. All the remaining units are in their vibrationless ground states. Three, four, and higher particle states with three or more monomer excitations (electronic plus vibrational) can also be included. However, the basis set grows exponentially with increasing number of units. Fortunately, for most practical applications, accurate solutions can be obtained by truncating the multiparticle basis set to contain only one and two particle states. The total number of vibrations, v_{max}, is capped to a maximum of 4 which is sufficient to obtain converged absorption and emission spectra.[219,251] Within the two particle approximation, eigenstates of Eq. 1 can be expanded in the local basis as,

$$|\psi_\alpha\rangle = \sum_{n} \sum_{\tilde{v}=0,1,..} c^{\alpha}_{n,\tilde{v}} |n,\tilde{v}\rangle + \sum_{n,\tilde{v}=0,1,..} \sum_{n',\tilde{v}'=1,2,..} c^{\alpha}_{n,\tilde{v};n',v'} |n,\tilde{v};n'v'\rangle \tag{10}$$

Similarly, for diagonalizing the bipolaron Hamiltonian in Eq. 7, the α^{th} bipolaron state can be expressed as an expansion in the multiparticle basis set according to

$$\begin{aligned}
|\Psi_\alpha\rangle &= \sum_m \sum_{\tilde{v}_m=0,1,...} c^{(\alpha)}_{m,\tilde{v}_m}|m,m,\tilde{v}_m\rangle \\
&+ \sum_{\substack{m,n\\(n>m)}} \sum_{\tilde{v}_m,\tilde{v}_n} c^{(\alpha)}_{m,n,\tilde{v}_m,\tilde{v}_n}|m,n,\tilde{v}_m,\tilde{v}_n\rangle \\
&+ \sum_m \sum_{\tilde{v}_m} \sum_{l(\neq m)} \sum_{v_l=1,2,...} c^{(\alpha)}_{m,\tilde{v}_m;l,v_l}|m,m,\tilde{v}_m;l,v_l\rangle \\
&+ \sum_{\substack{m,n\\(n>m)}} \sum_{\tilde{v}_m,\tilde{v}_n} \sum_{l(\neq m,n)} \sum_{v_l=1,2,...} c^{(\alpha)}_{m,n,\tilde{v}_m,\tilde{v}_n;l,v_l}|m,n,\tilde{v}_m,\tilde{v}_n;l,v_l\rangle \\
&+ \;.... \qquad (11)
\end{aligned}$$

Here, $|m,m,\tilde{v}_m\rangle$ is the one particle state, since both the holes are located on the same site, m, with $\tilde{v}_m$ (> 0) vibrational quanta in the shifted potential well. $|m,n,\tilde{v}_m,\tilde{v}_n\rangle$ is the two particle state since the holes occupy sites m and n with $\tilde{v}_m$ and $\tilde{v}_n$ vibrational quanta in the excited shifted potential well. Accordingly, the $|m,n,\tilde{v}_m,\tilde{v}_n;l,v_l\rangle$ is the three particle state. Four and higher particle states can also be described accordingly. In a similar fashion, eigenstates of the Frenkel-Holstein charge-transfer Hamiltonian in Eq. 4 which composes of vibronically coupled Frenkel and charge transfer excitons, can be expanded in a multiparticle local basis as

$$\begin{aligned}
|\Psi_\alpha\rangle &= \sum_n \sum_{\tilde{v}=0,1,..} c^{\alpha}_{n,\tilde{v}}|n,\tilde{v}\rangle + \sum_{n,\tilde{v}=0,1,..} \sum_{n',\tilde{v}'=1,2,..} c^{\alpha}_{n,\tilde{v};n',v'}|n,\tilde{v};n'v'\rangle \\
&+ \sum_n \sum_{v^+=0,1,..} \sum_{s=\pm1,\pm2,...} \sum_{v^-=0,1,..} d^{\alpha}_{n,v^+;s,v^-}|n,v^+;n+s,v^-\rangle \qquad (12)
\end{aligned}$$

where the first two terms in Eq. 12 represent one and two particle Frenkel excitons similar to that in Eq. 10. The last term in Eq. 12, $|n,v^+;n+s,v^-\rangle$, denotes two particle charge separated state in which site $|n\rangle$ which hosts a cation has v^+ vibrational quanta in the shifted, excited potential well while site $|n+s\rangle$ which hosts an anion has v^- vibrational quanta in the shifted excited potential well.

The multiparticle basis set can be extended to describe multiple excitations such as biexcitons, trions, tripolarons, which are topics of ongoing investigation. It should be noted that the multiparticle basis set is, however, not a convenient basis set in the regime of strong electronic coupling since it requires the inclusion of higher particle states. In such cases, the exciton-phonon basis set, which has been successfully employed in earlier studies,[213,252–254] is a more appropriate basis set.

Defects

Inhomogeneous polarizing environments such as structural and lattice imperfections, that is ubiquitous in most organic and hybrid materials, can localize quasiparticles (i.e., electrons and holes) in deep traps. Different forms of common inhomogenities in materials can arise from variations in nearest-neighbor π-stacking distances and torsional angles within the functional groups of the molecular building blocks. Static defects in materials can be efficiently described by considering random distribution of Gaussian site energy fluctuations having a standard deviation σ.[255] The presence of defects in most materials have a profound effect on the spectral signatures and charge transport properties of organic and hybrid materials, and can be taken into account phenomenologically by incorporating diagonal and off-diagonal disorder in the model. The effective Hamiltonian describing defects can be written as

$$H_{defects} = \sum_{n} \Delta_n |n\rangle\langle n| + \sum_{m,n} \Delta J_{m,n} (|m\rangle\langle n| + |n\rangle\langle m|) \tag{13}$$

where Δ_n is obtained by selecting the energy fluctuations from a Gaussian distribution with standard deviation σ,

$$p(\Delta_n) = \frac{1}{\sqrt{2\pi}} \sigma \exp \frac{-\Delta_n^2}{2\sigma^2} \tag{14}$$

Similarly, $\Delta J_{m,n}$ refers to random deviations in the electronic couplings which arises due to random changes in the separation between neighboring units. As detailed in Refs. 220 and 251, the degree of disorder can be spatially correlated with the two extreme limits being long-range (i.e., infinite spatial correlation) and short-range (i.e., no spatial correlation). In the limit of short-range disorder, for every disorder configuration, every unit in the lattice is assigned a random energy from a

Gaussian distribution having standard deviation σ (Eq. 14). In the opposite extreme of long-range disorder, within each disorder configuration, all the units in the lattice are assigned identical energy detunings. Knapp have further shown that the long- and short-range disorder can be distinguished by tuning the spatial correlation length (l_0).[256]

Absorption

Since Sections 3 and 4 primarily discuss excitonic and polaronic photophysical signatures in organic and hybrid materials, we briefly discuss the absorption in the far to mid-IR and UV-vis spectral region. For both Frenkel excitons (FE), and polarons (p), the absorption spectrum corresponding to an ensemble of disordered lattice sites is generally expressed as

$$A_{FE(P)}(\omega) \equiv \left\langle \sum_i f_i^{FE(P)} W_{LS}[\hbar\omega - (E_i - E_G^{FE(P)})] \right\rangle_C \tag{15}$$

where the bracket $\langle \ldots \rangle_C$ represents an average over an ensemble of disorder configurations, and the oscillator strength, $f_i^{FE(P)}$, is given by

$$f_i^{FE(P)} = (E_i - E_G^{FE(P)}) |\langle \psi_i | \hat{M}_{FE(P)} | G_{FE(P)} \rangle|^2 \tag{16}$$

Here, $|G_{FE(P)}\rangle$ is the ground-state wavefunction of both polarons and excitons with energy E_G, and the sum extends over all one-exciton or one-polaron eigenstates, $|\psi_i\rangle$, with energies, E_i, found through the diagonalization of the total Hamiltonian in Eq. 1. In the case of Frenkel excitons, the transition is from a ground state which contains no excitons to a state which contains single excitons. In the case of polarons, the transition instead takes place from a ground state, which already contains a hole, to an excited state which contains a hole. Therefore, the ground state in the case of a polaron is the lowest eigenstate of the Hamiltonian in Eq. 1. Hence, Frenkel excitons absorb in the UV-vis, while polarons absorb in the mid-IR spectral region. Elaborate discussion regarding the optical properties of excitons and polarons within the MHF can be found in Ref. 251.

Multiparticle Holstein formalism

While excitons and polarons have received considerable attention, a detailed characterization of trion dynamics is important since trions play a central role in determining the luminescence properties of organic and inorganic semiconductors. Trions are bound three-body states that consist of two holes and an electron, and offer the unique possibility of manipulating the charge, spin, and excitation of organic and hybrid materials. Similar to the case in charge-transfer excitons, the multiparticle basis set used to analyze the Holstein Hamiltonian can be readily extended to include the three charged units, i.e., trion states, (Fig. 1a) with a variable distribution of local vibrational quanta. The MHF is not limited to the local coupling between between the electronic and the intramolecular vibrational mode as discussed in this section so far. A combined Holstein-Pierls approach analyzed using a basis set similar to the multiparticle basis set incorporates local and non local coupling to both the intra- and inter-molecular vibrational modes.[257] This extension of the basis set to include the intermolecular vibrational mode, albeit only for a dimer, has successfully reproduced the measured absorption and emission spectrum of covalently linked dimers of bis(perylene diimide).[258,259]

Photophysics of Excitons

Excitons in Organic Materials

Several research groups have successfully employed the strategy of aligning donor (D) and acceptor (A) building blocks in order to modulate the optical, magnetic, and transport properties of various COF structures. Since providing a comprehensive analysis of the optical properties of D-A COFs is not the goal of this section, we only focus on selected photophysical signatures in the UV-vis energy region and emphasize direct correlations between the spectral features and potential applications including photothermal activity, electrochromism, light harvesting, framework stability, nature of aggregation, and energy and charge transport. Within this context, an important research question can thus be raised: *Is it possible to unravel the complex interplay among electronic coupling, vibronic coupling, electrostatic interactions, and different forms of defects through the interpretation of well defined spectral signatures?* More specifically, can distinct spectral signatures be identified that can be used as efficient screening protocols for synthesizing new COF-based structures for desired applications?

Effect of Aggregation: Theoretical investigations of the correlations between the nature of aggregation (H- vs. J-aggregation) in COFs and the UV-vis spectral response remains largely unexplored. Distinct optical signatures for H- and J-aggregation, based on the Frenkel exciton theory,[260,261] which involves the point dipole approximation of Coulomb coupling, was first introduced by Kasha.[262–266] In the case of H-aggregation where the transition dipole moments between the adjacent chromophores maintain a "side-by-side" arrangement, Coulomb coupling is positive and results in a blue shift of the main absorption peak compared to the absorption of the monomeric unit. In J-aggregates, the dipoles in the adjacent chromophores maintain a "head-to-tail" arrangement that leads to a negative Coulomb coupling and, consequently, a red shift of the main absorption band compared to the monomer.[262,264] Highly crystalline solid-state J-aggregate imine-linked COFs, which not only enable prolonged lifetime of singlet excitons but also facilitate exciton delocalization and stabilization of the excited species, have been synthesized by the Bein group.[267] The incorporation of porphyrin and thienothiophene units as molecular building blocks result in the formation of J-aggregate stacks having unprecedented COF domain sizes (up to 100 nm). H-aggregate COFs exhibiting high charge mobility have also been reported.[268]

While 2D COFs are usually described as eclipsed layered structures, experimental and computational studies have provided convincing evidence that the layers are slightly offset from one another.[269–276] Moreover, relatively broad peaks in the powder X-ray diffraction patterns do not rule out the possibility of small offsets in the inter-layer stacking arrangement.[277] Apart from the usual Kasha signatures that predict aggregation-induced spectral shifts between Coulombically coupled chromophores, additional vibronic signatures that can be used to differentiate between H- and J-aggregates were introduced by Spano.[146] In particular it was shown that the ratio of the first two vibronic peaks referred to as A_1 (0-0) and A_2 (0-1) decreases with increasing exciton bandwidth for H-aggregates but increases for J- aggregates.[146] Kasha's rule for optical spectroscopy assumes that the electron overlap between light absorbing neighboring chromophores must be small.[264] While long-range intermolecular Coulomb coupling predicts aggregation-induced blue and red shifts for H- and J- aggregates, respectively, such a scheme breaks down in closely π-stacked systems, due to significant wavefunction overlap and the emergence of short-range intermolecular charge transfer (ICT) between the neighboring chromophores.[145,219] In these scenarios, mereley relying on the spectral shifts may be misleading, and the nature of aggregation can be reliably predicted from the evolution of the vibronic signatures in the absorption and emission spectral lineshapes in the UV-vis energy region.

Theoretical simulations based on the MHF that explicitly includes short-range ICT have shown that the simultaneous presence and competition between long-range Coulomb coupling and short-range superexchange contributions result in a rich array of possible aggregate types (H-H, H-J, J-H, and J-J aggregates) with contrasting photophysical signatures and transport properties.[145] For instance, constructive and destructive interference between long- and short-range coupling determines exciton mobilty as well as exciton splitting (i.e., the rate at which excitons dissociate into charges). H-J aggregation has been extensively investigated in the case of conjugated polymer films and molecular aggregates.[278–286]

The experimental realization of H- and J-aggregation in COFs was observed in COF-5 that exhibits large exciton diffusion lengths.[140] While a red shift was observed in the absorption spectrum of COF-5, which indicates J-type aggregation, the change in vibronic ratios in the emission spectrum suggested a H-type coupling.[140] Such H- and J-aggregation signatures in COFs have been previously reported in literature, but have been rarely discussed in detail. For example, perfectly stacked COF structures were synthesized by the Jiang group by mixing pthalocyanine units with benzene diboronic acid.[268] Owing to the well-ordered arrangement of the π-stacked phthalocyanine units, the semiconducting NiPc COF exhibits enhanced light-harvesting capability in the visible and near-IR spectral regions, which facilitates efficient charge carrier transport. Al-

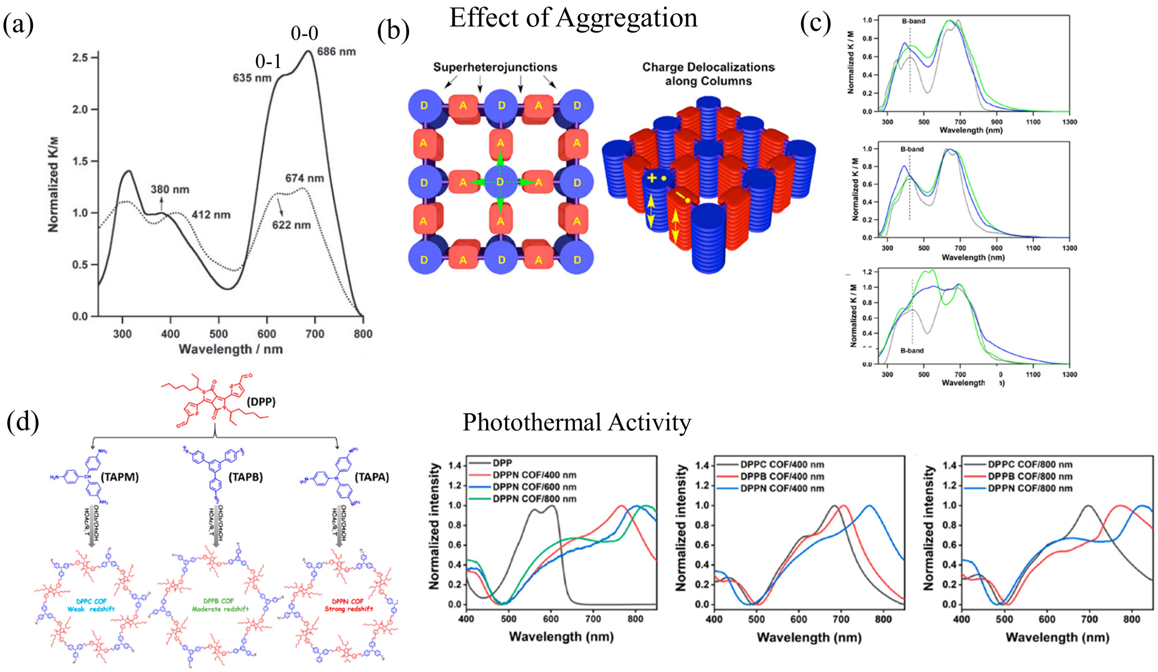

Figure 2: (a) H- and J- type bands observed in UV-vis absorption of NiPc COF (solid black). Although referred to as H-aggregates, the ratio of the intensities of the vibronic peaks I_{0-0}/I_{0-1} is greater in NiPc COF compared to the (MeO)$_8$PcNi monomer (dotted black) suggesting J-type aggrgation[268] (copyright 2011 John Wiley & Sons, Inc). (b) Schematic of segregated bicontinuous π-columnar arrays observed in COFs.[288] (c) UV-vis observation observed in D$_{\mathrm{MPc}}$-A$_{\mathrm{DI}}$ COFs also display H- and J- type signatures in the UV-vis.[288] (d) UV-vis absorption of DPP-based donor-acceptor COFs directly correlates with the COF particle size.[47] Figs. b,c reprinted with permission from Ref. 288. Copyright 2015 American Chemical Society, Fig. d reprinted with permission from Ref. 47. Copyright 2021 American Chemical Society

though referred to as H-aggregate, the UV-vis absorption spectrum of NiPc COF displays J-type aggregation signatures. In particular, in the absorption spectrum of NiPc COF (Fig. 2a), the absorption band at 380 nm, also referred to as the B band, is blue-shifted by 32 nm compared to the monomer precursor [(MeO)$_8$PcNi]. While this blue shift indicates the formation of pthalocyanine H-aggregates within the stacked COF structure, the Q bands of the NiPc COF, which are observed at 635 and 686 nm, are red-shifted by 12 nm from those of the [(MeO)$_8$PcNi] monomer. More importantly, the ratio of the intensities between the 0-0 and 0-1 vibronic peaks is larger in the case of the NiPc COF compared to the monomer, which is a well defined signature of J-aggregation.[287]

In Ref. 288, the Jiang group used electron-donating metallophthalocyanines and electronaccepting diimide derivatives as building blocks for the synthesis of D-A COFs (Fig. 2b), resulting in the formation of “super-heterojunctions” that display long-lived charge separation and exhibit remarkable photochemical properties. Electronic absorption measurements were performed to evaluate the interaction between the D-A units. Compared to the pthalocyanine monomeric units, the UV-vis absorption measurements of the COF structures (D_{CuPc}-A_{PyrDI}) displayed blue-shifted B bands, indicating H-aggregation. On the other hand, a red shift was observed in the low energy absorption bands of the COF structures compared to the imide building blocks, indicating J-aggregation (Fig. 2c). From the experimental observations, it was concluded that the COF structure is able to merge the absorption of the separate building blocks, which results in a broader absorption profile. However, in-depth theoretical investigations may provide new insights since perylene diimide (PDI) aggregates alone display two asymmetrically broadened absorption bands on transformation from one aggregate form to the other, with one band being red shifted and the other being blue shifted relative to the absorption of the monomeric unit.[218,289–294]

In this context, the steady state absorption and emission spectra of two PDI derivatives were theoretically investigated using the Frenkel-CT/Holstein Hamiltonian.[243] Simulations using the MHF were able to reproduce all the salient spectroscopic signatures of both the PDI derivatives. It was concluded that the band splitting observed in PDI aggregates primarily arises due to the coupling between Frenkel and charge-transfer excitons in the resonant regime, which is driven by intermolecular electron and hole transfer. Theoretical investigations based on the MHF in Ref. 243 also shed light on how the vibronic spectral features of the two main bands in the UV-vis absorption of PDI aggregates are governed by the interplay between long-range Coulomb coupling and short-range superexchange CT-mediated couplings.

H- and J-type aggregation was recently reported in highly luminiscent TAT COF, which was described as non-fluorescent J-type class of aggregates.[141] These studies suggest that the existence of possible correlations between the photophysical response of COFs and the nature of aggregation or interlayer packing arrangement needs more detailed theoretical investigations.

Effect of Particle Size: In a recent study, Schiff-based reactions were used to synthesize a series of size-controllable nanoscale COFs (DPPC, DPPN, DPPB) with uniform and spherical morphology.[47] This was achieved by incorporating D-A building blocks based on Diketopyrrolopyrrole(DPP) units, which resulted in a broad absorption profile that extended into the near-IR energy range as shown in Fig. 2d. In addition, the UV-vis spectral response shows a positive correlation with the size of the COF particle, with the maximum of the absorption spectrum red-shifting from 768 to 824 nm as the particle size increases from 400 nm to 800 nm. Interestingly, besides the observed red shift relative to the DPP building block, the spectral lineshapes of the corresponding COFs dramatically differ with increasing particle size and display the emergence of a featureless broad peak centered around 600 nm (Fig. 2d).

Electrochromism: Electrochromism is a property that describes reversible color changes of a material in response to an externally applied electric current. The Bein group paired highly electron deficient isoindigo-based building blocks with electron-rich pyrene motifs to synthesize highly crystalline imine linked D-A COFs that absorb light throughout the visible and near-IR energy range.[295] The absorption spectrum of the COF films displays a dominant near-IR band followed by a lower-intensity UV–vis band at a higher energy. A red shift in the absorption spectrum was observed depending on the choice of the molecular building blocks.[295] In a follow-up study using similar D-A-D motifs and incorporating modified thienoisoindigo building blocks, Bessinger et. al. synthesized a series of highly efficient, fast-switching, and stable electrochromic 2D COFs as shown in Fig. 3a.[296] Positive correlations between the spectral changes in the UV-vis and near-IR response and electrochromic properties were reported. The electrochemical oxidation of py-ttTII COF was associated with the bleaching of the main absorption bands in the neutral COF structure which was accompanied by the simultaneous emergence of new spectral features in the near-IR energy range (Fig. 3b). The first and second oxidation steps produced spectral features at 1000 and 900 nm which were attributed to the formation of polarons and bipolarons, respectively. These results suggest that it would be useful to uncover spectral signatures that can be efficiently used to differentiate polarons, bipolarons, and excitons in neutral and oxidized COF structures.

Effect of Relative Humidity: Li et.al. reported a strategy for engineering the bandgap of 2D

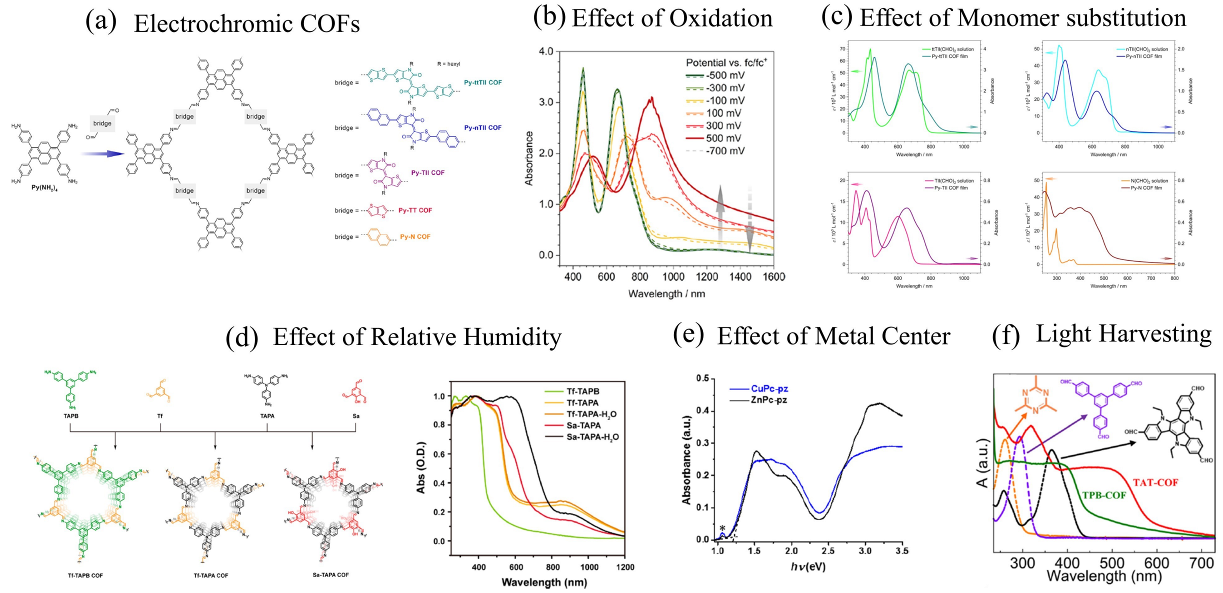

Figure 3: (a) Example of electrochromic COFs synthesized by the Bein group.[296] UV-vis spectral features of D-A COFs as a function of (b) oxidation,[296] (c) monomer building blocks,[295] (d) relative humidity,[297] and (e) metal centers.[298] (f) UV-vis absorption spectram of highly emissive D-A COFs.[141] Figs. a,b reprinted with permission from Ref. 296. Copyright 2021 American Chemical Society. Fig. c reprinted with permission from Ref. 295. Copyright 2017 American Chemical Society. Fig. d reprinted with permission from Ref. 297. Copyright 2018 American Chemical Society. Fig. e reprinted with permission from Ref. 298. Copyright 2019 American Chemical Society. Fig. f reprinted with permission from Ref. 141. Copyright 2021 American Chemical Society

COFs by introducing D-A units into the COF framework.[297] Triphenylamine and salicylideneaniline building units were used to synthesize 2D COFs that exhibit eclipsed stacking arrangement and excellent nonlinear optical limiting behavior. It was also found that the UV-vis spectral signatures of the COF structures were sensitive to the adsorption of moisture. In order to monitor the correlations between the spectral response and band-gap narrowing, the UV-vis measurements were performed as a function of relative humidity. While the absorption spectrum for dry or fully wetted TF-TAPA COF remained unchanged with increasing relative humidity, the absorption spectrum for Sa-TAPA further red-shifted to the near-IR energy range, with distinct color change from red to black (Fig. 3d). This red-shift was attributed to conformational changes in the framework which was further confirmed by FT-IR and NMR studies. The observed sensitivity of the UV-vis spectral signatures to the uptake of moisture and stability of the COF structure emphasizes the importance of investigating the role of structural and conformational disorder on the photophysical response of COFs as well as how disorder affects the electronic properties of COFs.

Effect of Metal Center: In order to investigate the effect of metal centers, two structurally and morphogically similar π-conjugated 2D COFs based on Zn- and Cu-phthalocyanine macrocycles and pyrazine linkers were synthesized by Wang et. al.[298] Although the incorporation of different metal centers results in distinct spectral signatures in the UV-vis as shown in Fig. 3e, it was demonstrated that changing the metal center from Zn to Cu in the pthalocyanine moiety has negligible effect on the charge carrier transport properties, with the hole mobility being negligible along the COF plane and finite between the COF planes.

Light Harvesting: Two highly emissive, fully conjugated D-A sp^2-C-COFs were recently synthesized by Yang et. al who showed that the exciton relaxation pathway and photoluminiscence quantum yield were controlled by planarity, conjugation, and interlayer aggregation.[141] Using a combination of experimental and TDDFT calculations, direct correlations were established between the COF structure and associated light harvesting properties, charge transfer, emission quantum efficiency, and photophysical signatures (Fig. 3f). In particular, it was emphasized that in order to have a better understanding of excitonic effects in COF structures, it is crucial to consider the contributions from superexchange ICT coupling as discussed earlier in this section.

The experimental studies discussed above demonstrate that COFs display specific photophysical properties that are extremely sensitive to various factors, including the nature of the building blocks, relative humidity, inter-layer packing arrangement and/or type of aggregation, particle size, and defect density. The characteristic UV-vis spectral signature for most D-A COFs is the presence of a lower energy band (B band), typically starting at 500 nm and extending into the near-IR energy range, accompanied by a higher energy band (Q band) between 300 nm to 500 nm. However, as shown in Fig. 2 and Fig. 3, these spectral features can vary significantly for different COF structures. For example, the relative intensities of the near-IR and UV-vis bands can be different for various COF structures. Unlike most COFs that do not display a vibronic structure in either of the two bands, the NiPc COF displays a pronounced vibronic structure in the Q band as shown in Fig. 2a. The spacing between the two vibronic peaks in Fig. 2a is approximately around 1200 cm^{-1} and can be associated with the coupling between the Frenkel excitons and the aromatic to quinoidal stretching mode of the framework. In order to elucidate structure-photophysics relationships in COFs, it is necessary to develop an in-depth understanding of the factors that govern the relative intensities of the B and Q bands, the separation between the maximum of the two absorption bands, the broadening of the bands, and the vibronic features. It is equally important to investigate the role of Frenkel and charge transfer excitons as well as electron-phonon coupling on the photophysical signatures of various COF structures.

In this context, Qarai et. al. have recently introduced a vibronic exciton model based on the MHF for a D-A-D arrangement of chromophores which was used to simulate the steady state absorption spectrum of push-pull low band gap D-A copolymers.[287] The MHF adopted in Ref. 287, that includes Frenkel-like and charge separated electronic states, and, more importantly, vibronic coupling (involving the aromatic to quinoidal stretching mode) on equal footing, accurately reproduces most of the salient spectroscopic features in the measured absorption spectra of PffBT4T copolymers. Fig. 4 shows that a similar Holstein-style Hamiltonian developed with parameters

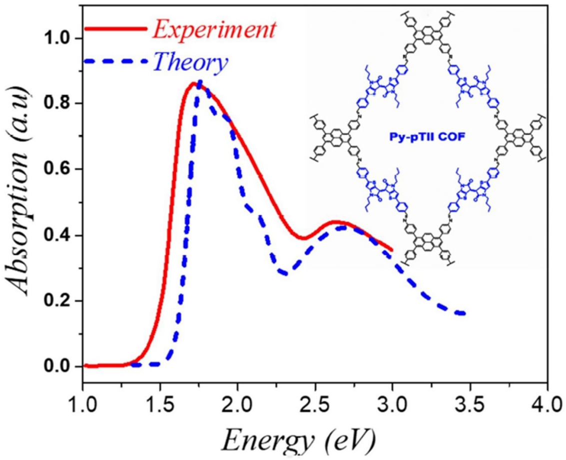

Figure 4: Comparison of the simulated spectrum using the MHF with the measured absorption spectrum of pyptII COF replotted from Ref. 295.

obtained from the DFT calculations of Ref. 287 accurately reproduces the experimental spectrum of the pyptII COF reported in Ref. 295. Analogous to the case in 1D copolymers, good agreement between the measured and simulated absorption spectra of pyptII COF was obtained using a single chain with an alternate sequence of coupled donor and acceptor building blocks. A comparison between the experimental absorption spectra of low band-gap D-A COFs and copolymers reveals that the spectral features in both D-A COFs and copolymers are quite similar. However, unlike in the case of PffBT4T, the absorption spectrum of the pyptII COF does not display the pronounced vibronic structure in the low-energy Q band. The vibronic features in pyptII COF are most likely obscured by the presence of inherent electronic and structural defects.

The close similarity between the absorption spectra of COFs and copolymers suggests that inter-framework interactions may be of secondary importance in the case of pyptII COF although some caution should be used before applying this conclusion to all D-A COFs since other factors may also affect the optical signatures of these materials. For example, the physical mechanisms responsible for the the emergence of a featureless peak centered at $\sim$630 nm (Fig. 2d), which broadens with increasing particle size of the COF films or increasing electron donating ability of the monomer units in DPP-based COFs,[47] are not well understood. In addition, while most D-A COFs usually display two absorption bands, such spectral signatures disappear in the case of Py-N COF (Fig. 3c),[296] TAT-COF (Fig. 3f), and TPB-COF[141] where the usual two-band spectrum is replaced by a much broader featureless peak. Finally, unlike the usual assumption that the low (high) energy band can be readily attributed to intermolecular charge transfer ($\pi - \pi^*$ transition), the MHF analysis indicates that both the bands have partial CT character and arise from the efficient mixing between Frenkel- and CT-type excitations.[287]

Building upon the 3D Holstein polaron model recently developed to investigate the effects of defects, domain size, chemical doping, and topology on the mid-IR photophysical signatures and charge transport properties of COFs,[216,217] future studies should go beyond a simple single chain analysis and focus on developing 3D vibronic exciton models for various COF topologies. Explicit inclusion of intra- and inter-framework electronic interactions, Frenkel and charge separated exciton states, and strong electron-phonon coupling on equal footing is necessary to investigate the spectral changes in both the UV-vis absorption and emission lineshapes of COFs. Furthermore, due to poor crystallinity and high defect density present in porous frameworks such as COFs, it is necessary to incorporate the effects of different forms of structural and conformation defects in our future studies.

To provide a detailed understanding of the factors that govern the photophysical response of COFs, it would be important to break down the problem by reducing the frameworks into their isolated monomeric components, which would allow for a systematic analysis of the evolution of the UV-vis spectral signatures from the isolated monomeric units to the aggregated monomers and aggregated 3D frameworks. This systematic analysis would provide direct comparisons between the spectroscopic signatures of the aggregated COF structures and the aggregated monomers. Such an analysis is particularly relevant since the UV-vis spectra of some COF films appear to be the mere superposition of the absorption spectra of the corresponding building blocks.[299] By developing consistent theoretical interpretations of the experimental measurements available for various COFs, it will be possible to gain insights into how functionalizing or modifying the chemical composition of the individual building blocks affects the nature of aggregation, stability, and both the photophysical and energy transport properties of these materials.

Excitons in Hybrid Materials

As in organic materials, UV-vis absorption and emission processes in hybrid materials are governed by delocalized excitations.[129–133,300] However, unlike organic materials where Frenkel and CT excitons are the predominant form of excitations, photoexcitation of hybrid materials result in the formation of Frenkel and Wannier-Mott excitons associated with the organic and inorganic components, respectively.[301] Frenkel excitons are bound electron-hole pairs localized on a single unit cell, while Wannier-Mott excitons are characterized by a much larger Bohr radius and consist of an electron and a hole that can be tens of unit cells or molecules apart.[302] Wannier-Mott excitons therefore experience a much smaller Coulomb binding energy (< 100 meV) compared to

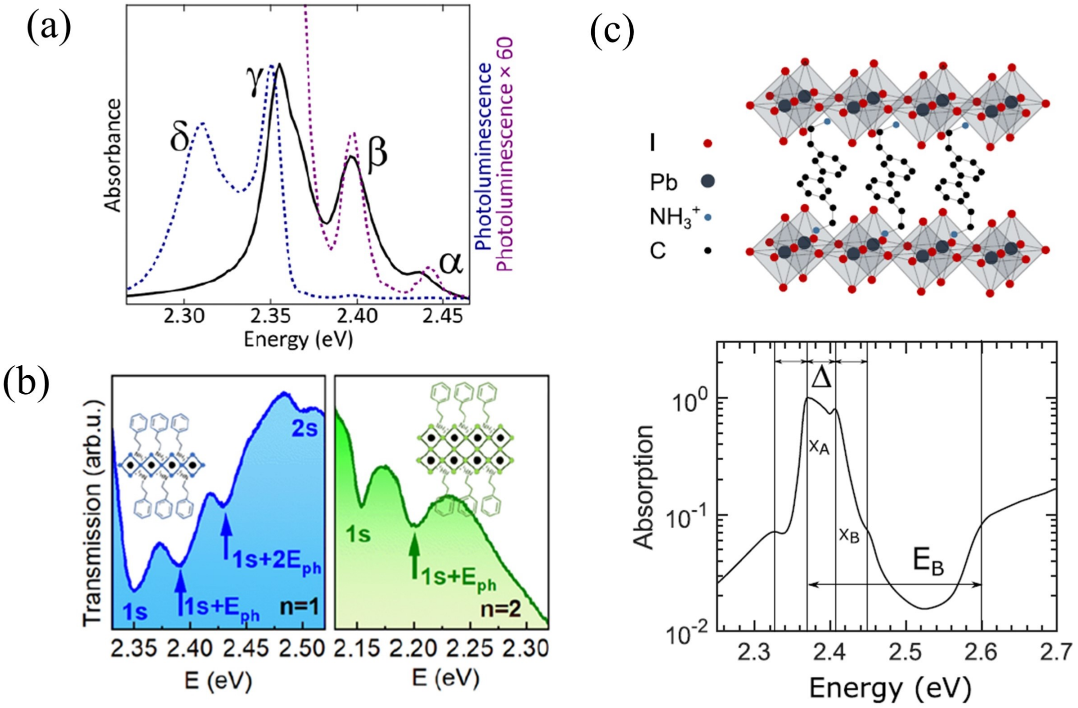

Figure 5: (a) Exciton fine structure observed in the absorption (solid black) and emission spectrum (dotted black) of phenethylammonium lead iodide.[152] (b) Transmission spectra of n=1 and n = 2 thin films of $(PEA)_2(CH_3NH_3)_{n-1}Pb_nI_{3n+1}$ at 4K.[305] (c) Linear absorption spectrum of $(PEA)_2PbI_4$ at 5K.[235] Fig. a reprinted with permission from Ref. 152. Copyright 2016 American Chemical Society. Fig. b reprinted with permission from Ref. 305. Copyright 2020 American Chemical Society. Fig. c reprinted with permission from Ref. 235. Copyright 2020 American Chemical Society

Frenkel excitons ($\geq$ 500 meV).[303] Since hybrid materials like MOFs and perovskites consist of organic and inorganic building blocks, both Frenkel and Wannier-Mott excitons may co-exist upon photoexcitation.[233,304]

The origin of the excitonic fine structure that is observed in the absorption and emission spectra of 2D perovskites[152,153,234–236,305–307] is currently a topic of ongoing debate. Multiple equally spaced peaks are found in the absorption and emission spectra of $(PEA)_2PbI_4$ as shown in Fig. 5. Kagan and coworkers attributed the origin of the exciton fine structure, which has a spacing between 40 and 46 meV, to a vibronic progression arising from the coupling of the electronic transition to a distinct vibrational mode located in the organic cation (Fig. 5a).[152,153,234,306] Similar spacings of 35 meV to 40 meV were observed at low temperature in the measured spectrum for

$(PEA)_2PbI_4$ as shown in Fig. 5c, and were attributed to distinct excitonic peaks by Silva, Srimath and coworkers.[235,236] The peak at approximately 40 meV in $(PEA)_2PbI_4$ was attributed to Rashba splitting.[308] A recent study has attributed the exciton fine structure observed in the photoluminscence spectrum of $(PEA)_2PbI_4$ to exciton-polaron emission.[309]

Most perovskites synthesized to date incorporate small organic cations such as methyl-, phenethyl-, or butylammonium as organic spacers. Strauss, Kagan, and coworkers have extensively investigated the role of small organic cations in tailoring the electronic and optical properties of 2D lead halide perovskites.[153,234,306] It was found that single atom substitution on the organic cation dramatically alters the steady-state absorption and emission spectra as shown in Fig. 6a.[153] It was also found that longer organic cations are associated with greater energetic disorder which obscured the presence of the vibronic fine structure in both the absorption and emission spectra (Fig. 6b), and results in a blue-shifted excitonic absorption.[306] Mitzi and coworkers have synthesized perovskites that incorporate oligothiophene cations of various lengths to investigate the role

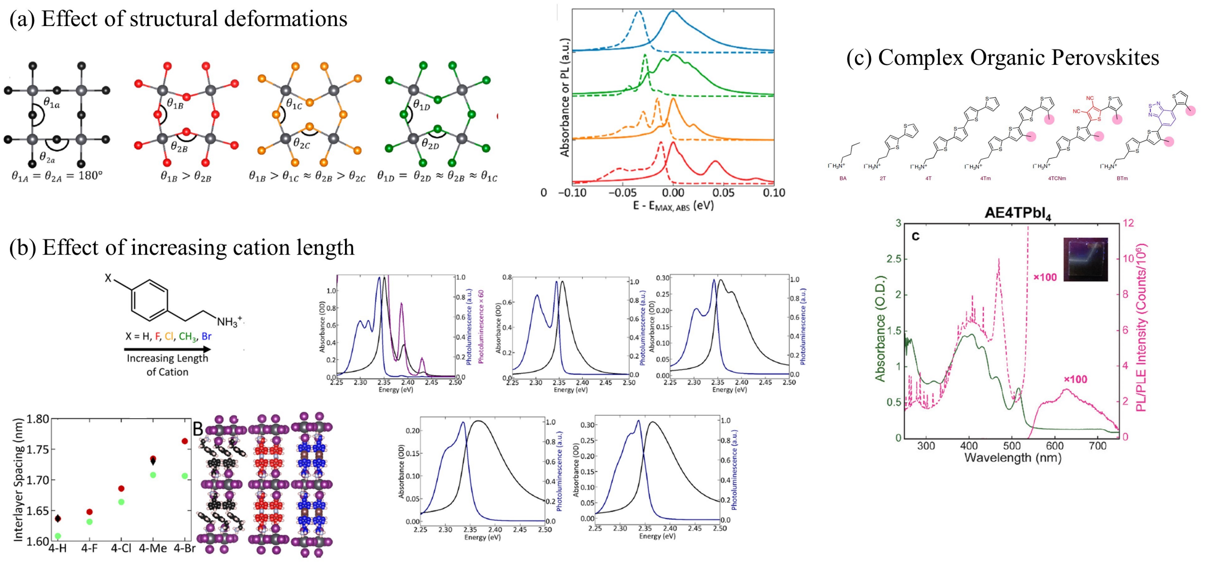

Figure 6: (a) The exciton fine structure in the UV-vis absorption and emission spectrum in perovskites changes as a function of structural deformation[153] or (b) increasing length of the organic cations.[306] (c) Vibronic progression observed in the UV-vis absorption spectrum of $(AE4T)PbI_4$.[233] Fig. a reprinted with permission from Ref. 153. Copyright 2020 American Chemical Society. Fig. b reprinted with permission from Ref. 306. Copyright 2019 American Chemical Society

of long and bulky organic components on the photophysical properties and tailor the excited state dynamics of lead halide perovskites.[233,310] These perovskites incorporating longer organic cations have been referred to as “complex organic perovksites” .[233]

Spectral signatures of both Frenkel and Wannier-Mott excitons as well as electron-phonon coupling was observed in the absorption spectrum of (AE4T)PbI_4.[233] The UV-vis absorption spectrum shown in Fig. 6c exhibits a broad absorption peak centered at ∼400 nm which can be directly associated with the Frenkel exciton located in the organic component of the perovskite.[233] The shoulders between 380 nm and 480 nm were attributed to a vibronic progression that arises from the coupling of the Frenkel excitons to the aromatic to quinoidal vibrational mode in the oligothiophene units. The narrow peak centered at ∼520 nm was attributed to the formation of Wannier-Mott excitons. Fig. 7 show that simulations using the MHF reproduce the vibronic progression arising from the organic component in (AE4T)PbX_4 (X = Cl, Br, and I).[311] It was also found that the choice of the halide ion in the inorganic component plays a central role in determining the shape of the vibronic structure observed in oligothiophene based perovskites.[311] The observed trends in the experimental absorption spectra are a direct consequence of the confining environment provided by the inorganic framework as well as the variation of excitonic coupling that decrease from (AE4T)PbCl to (AE4T)PbI. The theoretical insights gained from Ref. 311 are quite relevant in the context of the debate surrounding the origin of the exciton fine structure. The

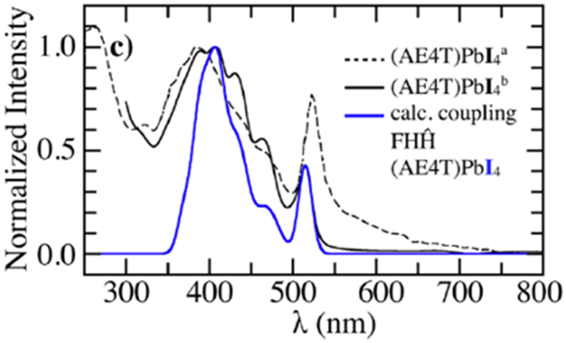

Figure 7: Comparison of the simulated spectrum using the MHF[311] with the measured UV-vis absorption spectrum of (AE4T)PbX_4 from Ref. 233 Reproduced from Ref. 311, with the permission of AIP Publishing.

transition spacings in the excitonic spectra seem to directly correlate with the choice of the organic spacer. While transition spacings of 14 meV and 40 meV were observed in the presence of aliphatic chains[312,313] and phenyl groups,[152,235,236,314] respectively, the presence of oligothiophene cations in (AE4T)PbX_4 results in a distinct progression having a transition spacing equal to the aromatic-to-quinoidal vibrational energy of $\sim$0.17 eV.

Despite rapid progress, several fundamental questions about the optical properties of perovskites still remain unanswered: a) How do structural changes (i.e., composition, length, and cross-Sectional area) induced by the organic cation influence the photophysical properties? b) What is the physical origin of the excitonic photophysics observed in 2D perovskites at low temperature? c) How do energetic disorder (in both organic and inorganic layers) and electron-phonon coupling affect the photophysical and transport properties of perovskites? d) Can spectral signatures be used to distinguish between Frenkel and Wannier Mott excitons in perovskites? While the theoretical model based on the MHF presented in Ref. 311 is a promising first attempt to investigate the absorption spectra and gain insights into structure-photophysics relationships in perovskites, future studies need to explicitly include the coupling between Frenkel and Wannier-Mott excitons to further disentangle the role of exciton-exciton coupling in the experimentally measured absorption and emission spectra. We hypothesize that strong organic-inorganic exciton coupling can impact the absorption spectra of perovskites and lead to changes in both the positions and linewidths of the spectral features, as well as changes in the vibronic progressions associated with the organic components. In this context, the MHF is ideally suited for such detailed analyses.

The formation of Frenkel and Wannier Mott excitons can also be quite relevant for MOFs. A recent study reported that the optoelectronic efficiency of semiconductive MOFs can be bolstered by efficient framework-guest interaction.[315] In particular, it was shown that the incorporation of electron-deficient guest molecules in the pores of a Terbium-based MOF results in significant energy transfer and facilitates the conversion of Wannier-type excitons into Frenkel-type excitons. Similar spectral signatures in the UV-vis energy region (i.e., multiple equally spaced peaks) to that observed in perovskites, were also observed in highly oriented thin films of triphenylene-based

MOFs.[316]

Distinct spectral features were found in MOFs where hexahydroxytriphenylene (HHTP) ligands are used in combination with different metal centers. In particular, the presence of Ni^{2+} and Cu^{2+} in the framework results in a spectrum displaying multiple equally spaced peaks in the range between 200 nm and 350 nm, and a broad absorption peak centered at $\sim$600 nm.[316] The series of multiple equally spaced peaks, however, disappears in the MOF structure with Fe^{3+} metal centers and is replaced by a broader featureless peak centered at $\sim$900 nm.[317] These observations suggest that the choice of metal centers impacts the local MOF structure and the corresponding spectral signatures. A close analogue of the HHTP ligand, hexahydroxy-tetraazanaphthotetraphene (HHTT), was recently used to synthesize π-conjugated 2D MOFs that display the characteristic vibronic signatures in the UV-vis energy range.[318] HHTT-based MOFs exhibit record high conductivities due to stronger inter-ligand interactions and a larger π-conjugated HHTT core compared to HHTP-based MOFs. Insights into the strength of the stacking interactions in MOFs can be gained from the analysis of the UV-vis absorption spectrum. Specifically, while the spectrum displays a distinct vibronic progressions when DMF is used as the solvent, this vibronic progression vanishes when water is used as a solvent. This suggests that using DMF as a solvent disrupts the (strong) π-stacking interactions and, hence, leads to larger MOF crystals (Ni_3HHTT_2) compared to when water is used a solvent.

It was also shown that metals favoring the square-planar (octahedral) coordination tend to form eclipsed (staggered) packing motifs in the corresponding MOF structures, which has a direct influence on the measured conductivity values. While Ref. 318 reported the successful synthesis of atomically precise MOF single crystals, obtaining such high-quality and large crystals is still rare. In the absence of high-quality MOF crystals, optical measurements, e.g., UV-vis absorption and photoluminescence, can be efficiently used to characterize the properties of MOFs structures. In this context, by providing theoretical predictions of the correlations among UV-vis spectral signatures, packing arrangements, nature of the organic ligands and metal centers, and transport properties, the MHF can provide fundamental insights that will help establish effective design principles for the development of new MOF structures with improved transport properties.

Photophysics of Polarons

Polarons in Organic Materials

Unlike neutral excitations (excitons) that absorb in the UV-vis energy range, charged excitations (polarons) absorb in the mid-IR energy range due to differing ground states and optical selection rules.[251] In the case of Frenkel excitons, the generally weak nature of the excitonic coupling between the nearest neighbors results in the formation of distorted vibronic progression having H- or J-like spectral signatures depending on the sign of the Coulomb coupling.[146,251] However, in the case of polarons, the much stronger electronic coupling (also referred to as transfer integrals) between the nearest neighbors obscures the vibronic structure in the mid-IR energy range. In the case of conjugated polymers, the values of the transfer integrals lie between 0.3 eV and 0.5 eV,[319] and are significantly larger than the values of the exciton couplings.[229,230,232] Furthermore, in contrast to UV-vis spectra originating from excitons, the mid-IR spectral signatures of polarons are insensitive to the sign of electronic coupling, implying there are no H- or J- type polarons.[251] The absorption spectral area for polarons decreases with increasing short-range disorder (i.e., there is no oscillator sum rule), which is reflective of a decreasing polaron coherence length. Therefore, unlike in the case of excitons, the mid-IR absorption spectrum can be efficiently used to extract the polaron coherence lengths. For excitons, one must instead resort to the photoluminiscence spectrum to extract the exciton coherence lengths.[320] The fundamental similarities and differences in the optical responses and quantum coherence lengths of excitons and polarons in organic materials as a function of electronic coupling, vibronic coupling, and short- and long-range disorder have been discussed in detail in Ref. 251.

The creation of polarons in semiconducting homo-polymers and donor-acceptor copolymers, either by photoexcitation (i.e., photoinduced absorption spectroscopy) or by doping (electrochemical or chemical), results in the appearance of new peaks in the mid-IR energy region, including a low-energy peak between 0.05 and 0.2 eV, and a broader high-energy peak between 0.25 and 0.9 eV.[220–222] The low-energy peak dressed with infrared active vibrational (IRAV) modes has been referred to as peak A,[220–222,251] DP_1(delocalized polaron),[321,322] or CT (charge transfer)[323–326] by different groups. The broader high-energy peak, referred to as peak B,[220–222,251] P_1,[321,322] or C_1[323–326] is mostly featureless. Polaron signatures with the characteristic A and B polaron peaks in the mid-IR energy range have also been observed in the iodine-doped imine-linked COF.[64]

The MHF for polarons, which is discussed in detail in Refs. 216,217,220–222,251 naturally accounts for the occurrence of both the A and B peaks. As shown in Fig. 10, the Holstein-type Hamiltonian, represented in a multiparticle basis set, successfully reproduces the spectral signatures of chemically doped “bound” polarons as well as electrically and optically generated “free” polarons in homopolymers, D-A copolymers, and COFs. More importantly, the MHF for polarons also identifies specific spectral signatures from which the generally anisotropic polaron coherence lengths (both along the chain/framework and stacking directions) can be quantitatively determined. As emphasized in recent studies on semiconducting polymers and COFs,[216,251] direct signatures of extended polaron coherence can be attributed to a red shift of the high energy peak B and an increase in the A/B peak intensity ratio. Knowing the coherence distribution in organic materials is critical since it allows for determining whether charge transport in organic materials is limited by a local property, such as polaron delocalization, or a mesoscale property, such as crystallite connectivity.

Effect of chemical doping: Chemical doping has proved to be an excellent strategy for improving conductivity in organic materials such as polymers and COFs. Iodine doping was shown to significantly increase the conductivity of TANG-COF from 1.6×10^{-5} S cm^{-1} to 1.0×10^{-2} S cm^{-1} in vacumm.[64] This sharp increase in conductivity was associated with an increase in the number of free spins and the emergence of the A and B polaron peaks in the mid-IR energy range. Similar to semiconducting polymers,[327,328] COFs were shown to exhibit up to ten-fold increase in electrical conductivity upon prolonged exposure to iodine.[63–72]

The preferential location of the dopant counteranion in the polymer matrix and the type of

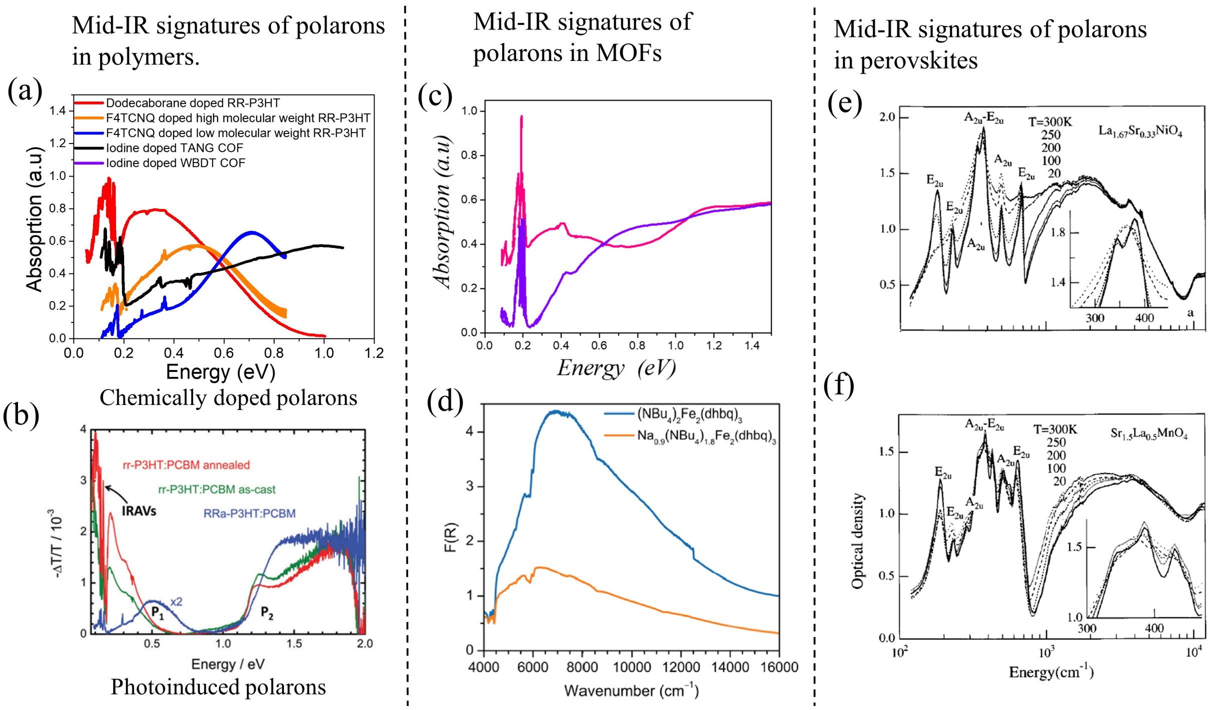
Mid-IR signatures of polarons in polymers.

Chemically doped polarons

Photoinduced polarons

Mid-IR signatures of polarons in MOFs

Mid-IR signatures of polarons in perovskites

Figure 8: (a) Mid-IR signatures of "bound" polarons in chemically doped polymers[221,222] and COFs[64,216] using data from Refs. 216,221,222. A red shift of the high energy peak B signifies enhanced polaron delocalization. (b) Mid-IR signatures of photoinduced polarons in conjugated polymers. (c,d) Mid-IR signatures of polarons in MOFs.[329,330] Panel (c) replotted from Ref. 329. Panel (d) reprinted with permission from Ref. 330. Copyright 2015 American Chemical Society (e,f) Mid-IR signatures of polarons in perovskites.[331] Copyright 1996 by American Physical Society. All rights reserved.

dopant also plays an important role in determining the final performance of both 2D COFs and 1D polymers. Additional valuable insights into the correlations among spectral signatures, dopant type, dopant location, polaron delocalization lengths, and conductivity can be obtained by comparing the mid-IR spectral signatures of iodine-doped TANG-COF with that of doped polymer films (Fig. 8a). In the case of F4TCNQ-doped P3HT films with low molecular weight (MW), the polarons are primarily localized on the polymer backbones with negligible interchain delocalization.[221] This is primarily due to strong Coulomb binding with the F4TCNQ counteranions that reside in the amorphous domains in close proximity to the polymer backbone (within ∼0.5-0.6 nm) , which results in hole localization. The blue curve in Fig. 8a shows that for the low-MW F4TCNQ-doped P3HT films, the location of peak B maximum is ∼0.7 eV and the A/B peak intensity ratio is ∼0.25. In marked contrast, doping high-MW P3HT films with F4TCNQ results in enhanced intra- and inter-chain polaron delocalization that is accompanied by a red shift of the B peak to ~0.5 eV and an increase in the A/B peak ratio to ~0.5 (orange curve in Fig. 8a).

The enhanced polaron delocalization in high-MW regioregular-P3HT is mainly attributed to weak Coulomb binding since the dopant counteranions in crystalline high-MW RR-P3HT films preferentially reside in the lamellar regions or in the amorphous domains of the polymer matrix and do not intercalate between the crystalline π-stacks.[332] Theoretical calculations based on the MHF predicted the approximate location of the counteranion in F4TCNQ-doped high-MW P3HT films to be within ~0.8-1 nm of the polymer backbone.[221] Interestingly, replacing F4TCNQ dopant with a bulky dodecaborane-based dopant, $DDBF_{72}$, was shown to yield significantly higher charge mobility in P3HT films, which was accompanied by an additional red shift of the B peak to ~0.3 eV and a further increase in the A/B peak intensity ratio to 1.25 (red curve in Fig. 8a). The increased mobility in $DDBF_{72}$-doped P3HT films[333] compared to F4TCNQ-doped P3HT films[221] is a direct consequence of increased polaron delocalization due to reduced electrostatic interactions between the dopant counteranion and the hole. Unlike F4TCNQ dopants, the reduced Coulomb binding in dodecaborane based dopants was due to a specific design which sterically protected the core electron density.[333] Combined experimental measurements and theoretical calculations based on the MHF showed that the $DDBF_{72}$ counteranions reside at ~1.8-2 nm from the polymer backbone.[222]

In the case of iodine-doped TANG-COF, the black curve in Fig. 8a display a significantly blue-shifted B peak with the maximum at ~1 eV. As expected, this large blue shift correlates to the iodine-doped TANG-COF exhibiting lower conductivity compared to semiconducting polymers and is a direct consequence of localized polarons due to strong Coulomb binding. In the case of polymers, the counteranions preferentially reside at a distance greater than 0.5 nm from the backbone depending on the choice of dopant type and MW of the polymer films. However, the presence of large pores in TANG-COF (and other COF structures) readily incorporates the counteranions, which results in shorter counteranion-framework distances (0.35 - 0.4 nm).[216] In turn, this leads to polaron trapping and, consequently, lower conductivity.

Spectral signatures similar to those discussed for chemically doped "bound" polarons are also evident in the absorption spectra of optically or electrically induced "free" polarons.[334] In this context, the absence of a chemical dopant or Coulomb binding implies enhanced delocalization of photoinduced polarons. As expected, Fig. 8b shows that the mid-IR signatures of photoinduced "free" polarons display a much red-shifted B peak at $\sim$0.22 eV and a larger A/B peak intensity ratio of $\sim$2 (Fig. 8b).

In a recent study, the Brinkmann group investigated the effects of different dopants on the charge transport properties of P3HT films.[335] It was found that preferential doping of the amorphous regions of the polymer films reduces polaron localization and improves charge transport as well as thermoelectric factors. Similar conclusions were reached from a systematic analysis of the effects associated with the counteranion size on polaron delocalization and mid-IR spectral signatures.[336]

Formation of free charge carriers was also observed in iodine-doped tetrathiafulvalene (TTF) COFs which resulted in high conductivity (2.8×10^{-5} S cm^{-1}).[63,66,337] The increase in conductivity measured in the TTF-ph COF was associated with increased delocalization of the polarons along the inter-layer π-stacking directions. We hypothesize that smaller pore sizes would lead to stronger electrostatic interactions due to closer proximity of the dopant counteranions present inside the COF pores and the holes present in the oxidized COF layers, which could result in trapped polarons and, consequently yield lower conductivity. In this regard, it should be noted that the TTF-ph COF, which is characterized by larger pores than the TTF-py COF, indeed exhibits higher conductivity.[337]

Effect of topology: Both exciton and polaron migration in COFs have been shown to depend on topological connectivity or lattice symmetry. Using a topology-templated polymerization strategy, the Jiang group successfully synthesized a series of fully sp^2 carbon-conjugated COFs having hexagonal, tetragonal, and kagome topologies.[34] The investigation of π-conjugation effect led to the important conclusion that the extent of exciton migration was controlled by lattice topology with an order of kagome $>$ tetragonal $>$ hexagonal. Analogously, the MHF for polarons was

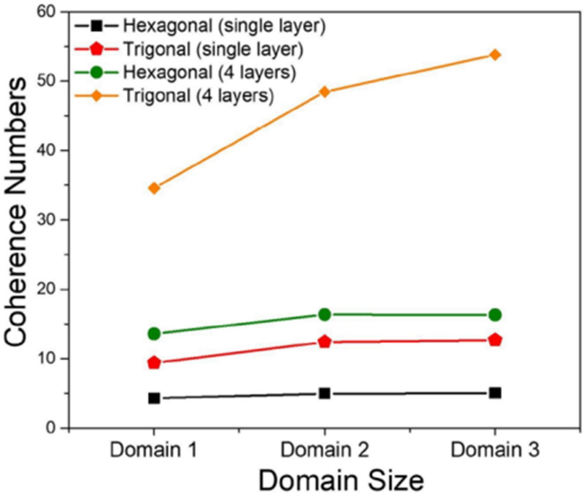

Figure 9: Intra- and inter-framework polaron coherence numbers as a function of topology of the COF structure. Trigonal COFs facilitate greater polaron delocalization compared to hexagonal COFs due to additional connecting pathways that help circumvent deep trap states and enhance hole mobility. Data is used from Ref. 217.

used to theoretically demonstrate that the extent of polaron migration both along the intra- and interframework directions follows the order trigonal/kagome $>$ tetragonal $>$ hexagonal.[217] It was theoretically demonstrated that polaronic transport in COF structures not only depends on the extent of π-conjugation and the strength of electronic coupling between the nearest neighbors but is also governed by the interplay between topological connectivity and presence of electronic defects in the framework. Ref. 217 further emphasized that the presence of additional connecting pathways in trigonal COFs compared to hexagonal COFs help circumvent deep trap sites and can therefore significantly enhance polaron delocalization by approximately three orders of magnitude in the case of layered COF structures (Fig. 9).[217] This theoretical prediction is indeed experimentally plausible since it was earlier shown that trigonal HBC COF exhibits higher mobility compared to other COFs having different topologies.[34]

This observation however does not hold in the case of doped COF structures. Upon chemical doping, the effect of topology is virtually nullified and the extent polaron delocalizaion is primarily determined by the location of the counteranion relative to the COF backbone and the strength of Coulomb binding. In the likely scenario of the dopant counteranions residing inside the COF pores and in close proximity to the framework backbone, the associated number of free charge carriers, extent of polaron delocalization, and conductivity will be low, independently of the framework topology.

Effect of interlayer stacking and disorder: 2D COFs potentially exhibit unique stacking arrangements by employing different molecular design principles which influence the photophysical response.[109,267,270–272,338–340] Interlayer stacking interactions strongly depend on various factors, including monomer's properties, planarity, crystallinity, stacking configuration (e.g., eclipsed vs. staggered vs. random), and hydrogen bonding. Different stacking arrangements such as cofacial vs. slip-stacked configurations directly influence the degree of charge transfer, polaron migration, and energy transfer along the π-stacks.[273,277,341,342] Strong cofacial interactions between the planar monomers with large π surface area experience significant wave function overlap between the stacks and facilitate more efficient polaronic hopping through the columns. Current investigations in our group are focused on characterizing spectral signatures in the mid-IR energy region for different packing arrangements in COFs.[273,277,341,342] In the eclipsed configuration, π-stacking maintains an "in-phase" registry where the donors line up with the donors and the acceptors line up with the acceptors as shown in Fig. 2b. In the segregated configuration, there is an "out of phase" registry where the donors line up adjacent to the acceptors. By extending the theory developed in Refs. 216, 217, 222 to the study of D-A COFs, we anticipate that the spectral signatures for different packing arrangements can be distinguished by analyzing only the mid-IR lineshapes. Using the same numerical techniques introduced in recent studies,[216,217,222] it is possible to evaluate the infrared spectrum polarized along the intra- and inter-framework directions. We anticipate that the resonant D-D and A-A interactions in the eclipsed form will facilitate greater delocalization of the hole along the inter-framework direction compared to the staggered arrangement. This greater delocalization of the hole in the eclipsed arrangement should also lead to a much larger polarization absorption component along the inter-famework direction compared to the intra-framework direction.

The charge carrier mobility was also studied as a function of film thickness in boronate esterbased COF thin films by the Bein group.[343] The hole mobility was found to be directly correlated with the thickness of the COF films, with thicker films being associated with significantly lower charge mobility, presumably due to the presence of electronic defects.

Polarons in Hybrid Materials

Mid-IR signatures of polarons in MOFs: Direct correlations between mid-IR signatures and conductivity is not limited to organic materials, such as polymers and COFs, but have also been reported in hybrid organic-inorganic frameworks, such as MOFs.[329,330,344–347] Ideally, MOF-based materials with high conductivity should enable efficient three dimensional charge delocalization within the framework. It was recently demonstrated that $\pi - \pi$ stacking interactions between the organic ligands alone can produce efficient charge transport pathways in MOFs, indicating that a metal-ligand bond with high covalent character is not a necessary requirement for achieving high conductivity.[329] By fine-tuning the inter-layer π-stacking distances between the organic 2D sheets in a series of lanthanide-based MOFs, the measured conductivity was found to be on par with the highest conductivity values reported for MOFs to date. The high conductivity was achieved despite negligible in-plane electronic communication and was solely attributed to out-of-plane charge transport. Although electronic structure calculations were used to determine the band structure and density of states of lanthanide-based MOFs, it would be important to further explore, at the fundamental level, the relationships between framework properties (e.g., flexibility and chemical nature of the organic ligands), measured conductivities, and mid-IR spectral signatures. Firstly, it is quite intriguing that a small decrease (0.005 nm) in the inter-layer stacking distance results in a significant increase (10^3) in the measured conductivity. Secondly, determining the origin of the mid-IR spectral features was deemed beyond the scope of the work and the origin of the mid-IR signatures were ambiguously assigned either to the presence of defects or metal/ligand vacancies and intra-ligand charge transfer (Fig. 8c). Interestingly, similar to the case in organic materials, spectral changes in the mid-IR energy range measured in Ref. 329 directly correlate with changes in the inter-layer stacking distances, choice of the metal centers, and measured conductivity. In particular, it was found that frameworks containing metals such as Holmium (Ho^{3+}) and Ytterbium (Yb^{3+}), which exhibit shorter π-stacking distances and higher conductivities, display a blue-shifted absorption (at $\approx$ 0.7 eV) compared to frameworks containing Lanthanum (La^{3+}) and Neodymium (Nd^{3+}), which exhibit longer π-stacking distances and lower conductivities (Fig. 8c).

Direct correlations between measured conductivity and mid-IR signatures were reported in $K_xFe_2(BDP)_2$ (BDP^{2-} = 1,4-benzenedipyrazolate) by Long and coworkers.[346] In this study, it was reported that fractional reduction of $K_xFe_2(BDP)_3$ results in a remarkable 10^4 fold increase in conductivity along a single crystallographic axis. It was also found that the greatest degree of electronic delocalization occurred at half reduction, resulting in a charge mobility of 0.29 $cm^2V^{-1}s^{-1}$. With increasing reduction and increase in charge mobility, the spectral features in the mid-IR energy range between 0.50 eV and 1 eV were found to grow in intensity until half reduction and then starts to diminish. The origin of the mid-IR absorption band was attributed to the formation of mid-gap polaron states.

Direct correlations between mixed valency, conductivity, and mid-IR spectral signatures were also reported in a 3D MOF composed of Fe^{III} centers and paramagnetic semiquinoid linkers synthesized by the Long group.[330] The intense blue curve in Fig. 8d was associated with significantly higher conductivity (0.16 S cm^{-1}) compared to the orange curve (0.0062 S cm^{-1}). However, the underlying physical mechanism behind the difference in spectral intensities was not directly investigated and the observed correlation between spectral intensity and conductivity was not elucidated. Similar low-energy spectral features were also observed in several redox-active MOFs and attributed to either intra-valence charge transfer or mid-gap polaron states.[344,345,347]

In order to lay the groundwork for future theoretical studies on MOFs, Fig. 10g shows that preliminary calculations carried out for lanthanide-based MOFs using the MHF for polarons adopted for COFs[216,217] qualitatively reproduce the spectral trends and lineshapes observed in Ref. 329. The MHF calculations shown in Fig. 10g were carried out for a hexagonal lattice consisting of four π-stacked layers, and the intra- and inter-framework couplings were set to 0.14 ev and 0.08 eV, respectively. Despite being in qualitative agreement with the experimental observations, the sim-

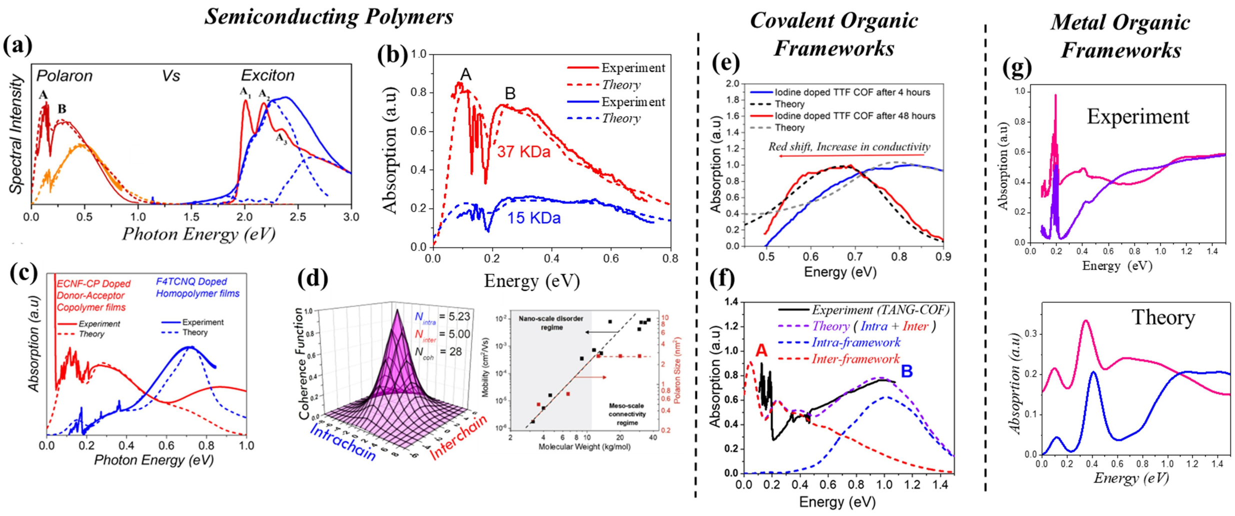

Figure 10: a) Left: Measured (solid) and simulated (dashed) MIR polaron spectra of dodecaborane[333] (brown) and F4TCNQ[221] (orange) doped P3HT films. Right: Measured (solid) and simulated (dashed) exciton UV-vis spectra for undoped P3HT films.[226,227,251] b) Measured (solid) and simulated (dashed) charge modulation spectrum of P3HT as a function of molecular weight.[220] c) Measured (solid) and simulated (dashed) charge modulation spectrum for a doped D-A copolymer and P3HT films.[221] d) Measured (solid) and simulated (dashed) photoinduced absorption spectrum for regioregular and regiorandom P3HT films.[222] e) Left: Polaron coherence function of 100% regioregular P3HT on a surface assembled monolayer with a molecular weight of 30 kg/mol. Intra- and inter-chain coherence numbers are shown in the inset.[224] Right: Correlation between polaron coherence and hole mobility as a function of the molecular weight.[224] (f,g) Measured (solid) and simulated (dashed) spectrum of iodine doped covalent organic frameworks.[216,217]Preliminary simulations using the MHF qualitatively captures the spectral trends of the MIR spectral signatures observed in lanthanide based MOFs replotted from Ref. 329. Data in panels a-f are from Refs. (216,217,220–222,224,251).

ulated spectrum is significantly blue shifted relative to the measured spectrum. This discrepancy is likely due to the neglect of the effects associated with the metal centers in the MOF structure. Furthermore, more accurate electronic couplings, which can be obtained from DFT calculations, are needed for a more reliable parameterization of the Hamiltonian. In this regard, the development of computational approaches for accurate calculations of the nearest-neighbor electronic couplings in hybrid materials such as MOFs are currently in progress.

Important future directions will be aimed at understanding, at a fundamental level, the origin of the low-energy spectral features, which can be tentatively assigned to intra-ligand charge transfer and the formation of delocalized polarons in the frameworks. The decrease in spectral intensity observed for 3D MOFs in Ref. 330, which is accompanied by a decrease in conductivity, is in good agreement with earlier observations for COFs[216,217] and semiconducting polymers,[220,221,251] suggesting that the observed drop in mid-IR oscillator strength is directly proportional to the decrease in the delocalization lengths of the polarons in the MOF structures. Based on this analogy with COFs/semiconducting polymers, it is therefore not surprising that higher spectral intensity is associated with higher conductivity in MOFs. However, detailed theoretical investigations are necessary for developing a consistent picture of the correlations between mid-IR signatures and polaron delocalization in different MOF structures.

Mid-IR signatures of polarons in perovksites: Studies of mid-IR absorption spectra on chemically doped perovskites date back to the 90s.[331,348] The correlations between the polaronic features in the mid-IR energy range and the transport properties and superconductivity were established in layered perovskites in Ref. 331,348. The spectral intensity and lineshapes of the mid-IR signatures were shown to be sensitive to polaron size, doping, and temperature. The similarity between the mid-IR signatures observed in chemically doped layered perovskites with general formula $La_{2-x}Sr_xMO_4$ (M=Ni, Mn, and Cu) and those observed in COFs, MOFs, and conjugated polymers is particularly striking.

The mid-IR band of perovskites consists of two main bands - a high-energy broad peak (peak B) and a low-energy peak (peak A) riddled with IRAV modes. Although not discussed by the authors, the position of peak B appears to correlate with the transport property of the perovskite structure. For example, $La_{2-x}Sr_xNiO_{4+y}$ (LSNO) either turns into a high temperature superconductor or displays metallic behavior, while $Sr_{2-x}La_xMnO_4$ (SLMO) always remains insulating at any value of x. The metallic behavior in LSNO was associated with a red shift of peak B and the band maximum occurred at 2000 cm^{-1} (Fig. 8e). On the other hand, the band maximum of SLMO is approximately around $\sim$4000 cm^{-1}(Fig. 8f). In addition, peak A also appears to grow in intensity for LSNO compared to SLMO.

These observations suggest that it would be important to connect specific spectral signatures of polarons, bipolarons, and polaron pairs with the nature of transport in perovskites (i.e., superconducting vs. insulating structures). In a recent study, mid-IR signatures of large polarons in 3D metal halide perovskites were investigated using a combination of first principles simulations and advanced spectroscopy techniques.[349] The mid-IR spectral signatures correspond to a dominant low-energy peak (referred to as P_0) centered at $\sim$0.06 eV, which was attributed to trap-state absorption, and a high-energy peak (referred to as P_1), which was attributed to mid-gap polaron states.[349]

The aforementioned experimental and theoretical studies demonstrate that the low-energy mid-IR spectral features contain key information about structure-property relationships and the extent of polaron delocalization in both organic and hybrid materials. In the case of perovskites, it would important to theoretically explore the correlations between the mid-IR signatures and the nature of transport (i.e., insulating or superconducting). Because of the similarity in the nature of defects and electronic structure, the MHF is ideally suited to connect the dots and help establish a thorough understanding of the polaronic signatures in organic and hybrid materials and establish direct correlations between mid-IR signatures with charge transport.

Conclusion

This perspective outlines the recent success and emphasizes potential future applications of the Multiparticle Holstein Formalism in understanding the photophysical and transport signatures of a diverse array of organic and hybrid materials. The MHF is based on a coarse-grained Holstein-style Hamiltonian in which electronic coupling, electron phonon coupling, electrostatic interactions, and different forms of long- and short-range defects are treated on equal footing, without invoking the Born-Oppenheimer approximation. A multiparticle basis set[206,219] is used to diagonalize the Holstein Hamiltonian where each basis function contains information about the location of the vibronically excited chromophore as well as additional purely vibrationally excited molecules. The MHF offers the possibility to "switch on and off" important contributions from electronic coupling, electron phonon coupling, defects, electrostatic interactions, etc., in a controlled manner that is typically unavailable to experiments. Taking advantage of these Hamiltonian-based "knobs", it is therefore possible to efficiently disentangle the important contributions from different experimentally relevant phenomena to the optical and transport properties of electronic materials.

We have recently shown that an expanded multiparticle basis set describing the Holstein Hamiltonian can be treated in a computationally efficient manner with the adaptation of vectorized code on multinode clusters, along with specialized sparse matrix algorithms.[216,217] Using this approach, we have explored large matrices and performed configurational averaging over thousands of realizations of disorder in a reasonable timeframe in order to obtain accurate assessments of the energy landscape, and obtain converged photophysical and transport properties of 2D porous materials such as COFs.[216,217] This advancement lays the foundation for future exploration of quasiparticles excitations, excited state processes, and photophysical and transport properties of a wide range of electronic materials that remains unaddressed to date, primarily due to computational limitations.

As demonstrated throughout this perspective, the MHF has the potential to make significant strides and advance our fundamental understanding in several important research directions. For instance, the incorporation of Frenkel, charge-separated electronic states, and vibronic coupling accurately reproduces the UV-vis absorption spectral features of low band gap copolymers and D-A COFs.[287] In the case of low band gap D-A copolymers, it was shown in Ref. 287 that single chains of alternating donor and acceptor chromophores behave just like J-aggregates due to the head-to-tail orientation of the interacting transition dipole moments corresponding to the donor and acceptor fragments. This J-type behavior is accompanied by an increased red-shift in the low-energy absorption band along with an increase in A_1/A_2 peak ratio, where A_1 and A_2 are the oscillator strengths of the first two vibronic peaks in the progression sourced by the symmetric aromatic to quinoidal vibrational mode. Interestingly, such an increase in the A_1/A_2 peak ratio was observed in NiPc COF compared to the monomer precursor (Fig. 2a). Examples of similar H- and J-type bands in COFs have been discussed in Section 3.1 and some caution therefore needs to be exercised before assigning the nature of aggregation in COFs. The inherent sensitivity of the UV-vis spectral signatures of D-A COFs to several important factors, including molecular packing, nature of aggregation, defect density, relative humidity, and oxidation have been highlighted in Section 3.1 which warrant further detailed theoretical investigations. The MHF is ideally suited to provide direct comparisons with available photophysical measurements in D-A COFs which will help determine how the intricate interplay between long-range Coulomb coupling and short-range CT-mediated couplings impacts the photophysical response and exciton dynamics in various COF structures.

We are especially excited about the applications to "hole" polarons in 2D COFs and 1D conjugated polymers where the theory has delivered a comprehensive account of the mid-IR spectrum of polarons that are generated either electrically or through chemical doping.[216,217,220–222,251,350] Importantly, the results are quite profound, especially with respect to the impact of short- and long-range disorder in defining the all-important spatial coherence lengths of polarons, a key quantity that determines the extent of nanoscale charge transport.[251] Recent theoretical and experimental studies have highlighted the importance of the position and size of the dopant counteranion in the polymer matrix in determining the charge transport and photophysical properties of COF films.[332,335,336] In this context, the coherence lengths of doped systems provide additional information about the possible location of the dopant counteranion within the polymer matrix.[216,251]

Although experimentally challenging, we envision that polarized mid-IR measurements on oriented samples will be a major breakthrough in the next decade. Polarized mid-IR measurements in conjunction with theoretical insights from the MHF will provide unambiguous understanding of the links between nanoscale transport with mesoscopic structure of different systems. Furthermore, establishing close connections between experiment and theory will help quantify the extent of three dimensional polaron delocalization and unravel the various factors that govern nanoscale polaron transport in semiconducting materials.

In the case of hybrid organic-inorganic materials, the MHF has successfully reproduced the trends in the vibronic progression observed in the UV-vis absorption spectra of AE4TPbX_4. In Ref. 311, the interactions between the organic and inorganic excitons in AE4TPbX_4 was assumed to be negligible. Despite this approximation, the theoretical study reported in Ref. 311 is an important first step since the presence of Frenkel excitons in the organic molecules typically display a broad absorption profile, containing a well-defined vibronic structure.[145,219] In order to provide an unambiguous interpretation of the excitonic photophysics in layered perovskites, future studies should include the coupling between Frenkel and Wannier-Mott excitons. To realize this goal, the behavior of the inorganic excitons can be described with a Wannier-Mott type Hamiltonian that accounts for electron and hole hopping, as well as Coulomb binding. As a first approximation, the vibronic coupling associated with the inorganic components in hybrid materials can be ignored since they are much weaker compared to their organic counterparts. However, the basis set can be extended to include multimode vibronic coupling originating from both the organic and inorganic components. Furthermore, the inclusion of both local and non local couplings to the intra- and inter-molecular vibrational modes may provide new theoretical insights into the formation of excimers in perovskites,[234] in a similar vein to what has been recently done for molecular dimers.[257] It should be noted that extending the analysis from molecular dimers to 2D perovskites will be computationally very challenging. In this regard, we believe that our recent efforts in extending the multiparticle modeling to large basis sets should be the preferred approach moving forward.[216,217] The MHF is also ideally suited to investigate how structural and conformational disorder present in the organic cations modulate the optical properties in layered perovskites. Similar to the studies that have been previously performed on organic materials,[219] we believe that a generic theoretical framework that considers the coupling between Frenkel and Wannier-Mott excitons, multimode electron-phonon coupling associated with the organic and inorganic components, respectively, and different forms of electronic and structural defects on equal footing will potentially establish direct comparisons with available experimental spectra in hybrid materials.[152,153,234,235,306]

To summarize, we believe that materials discovery for future technological applications cannot solely rely on the prediction of properties (band gap, charge densities, electronic couplings, oscillator strengths, etc.) calculated by quantum mechanical methods. In parallel with electronic structure modeling and machine learning methodologies, a comprehensive theoretical framework is needed that makes quantitative connections of the calculated properties with electronic, optical, and transport behavior of organic and hybrid materials. The future of materials modeling hinges on the synergistic integration of the HMF with electronic structure methods and data-driven techniques that will not only advance our fundamental understanding of the excited state processes but also provide unambiguous interpretations of well-defined spectral signatures that remain unexplored to date. Building upon the uniqueness and unparalleled accuracy of the MHF in reproducing conceptually complicated experimental data to date (see Figs. 7,4,10 and Refs. 219,221,222,243,251,257,287,311) it is possible to advance the community's fundamental understanding of quantum phenomena of many-body systems at the nanoscale. Furthermore, this integrated approach will contribute to the design rules for new device architectures for applications including but not limited to charge storage devices, photodetectors, and electrochromic sensors.

While state-of-the-art quantum chemistry techniques remain the preferred theoretical approach in chemical sciences, the MHF, which we believe is currently underrepresented in the literature, is a computationally inexpensive yet efficient alternative that can potentially decode puzzling experimental observations and transform the photophysical research landscape in the next decade.

Conflicts of interest

There are no conflicts to declare.

Acknowledgements

This research was supported by the National Science Foundation through grant No. CHE-1704063, and used the Triton Shared Computing Cluster (TSCC) at the San Diego Supercomputer Center (https://doi.org/10.57873/T34W2R) as well as resources of the Extreme Science and Engineering Discovery Environment (XSEDE), which is supported by the National Science Foundation through grant No. ACI-1053575. The software PETSc and SLEPc was used to diagonalize the Hamiltonian.[351–353]

References

(1) Tang, C. W.; VanSlyke, S. A. Organic electroluminescent diodes. *Appl. Phys. Lett.* **1987**, *51*, 913–915.

(2) Burroughes, J. H.; Bradley, D. D.; Brown, A.; Marks, R.; Mackay, K.; Friend, R. H.; Burns, P. L.; Holmes, A. B. Light-emitting diodes based on conjugated polymers. *Nature* **1990**, *347*, 539–541.

(3) Inganäs, O. Organic photovoltaics over three decades. *Adv. Mater.* **2018**, *30*, 1800388.

(4) Lee, H.; Park, C.; Sin, D. H.; Park, J. H.; Cho, K. Recent advances in morphology optimization for organic photovoltaics. *Adv. Mater.* **2018**, *30*, 1800453.

(5) Cheng, P.; Yang, Y. Narrowing the band gap: the key to high-performance organic photovoltaics. *Acc. Chem. Res.* **2020**, *53*, 1218–1228.

(6) Zhan, L.; Li, S.; Xia, X.; Li, Y.; Lu, X.; Zuo, L.; Shi, M.; Chen, H. Layer-by-layer processed ternary organic photovoltaics with efficiency over 18%. *Adv. Mater.* **2021**, *33*, 2007231.

(7) La Notte, L.; Giordano, L.; Calabrò, E.; Bedini, R.; Colla, G.; Puglisi, G.; Reale, A. Hybrid and organic photovoltaics for greenhouse applications. *Appl. Energy* **2020**, *278*, 115582.

(8) Park, S.; Kim, T.; Yoon, S.; Koh, C. W.; Woo, H. Y.; Son, H. J. Progress in Materials, Solution Processes, and Long-Term Stability for Large-Area Organic Photovoltaics. *Adv. Mater.* **2020**, *32*, 2002217.

(9) Li, D.; Yu, G. Innovation of materials, devices, and functionalized interfaces in organic spintronics. *Adv. Funct. Mat.* **2021**, *31*, 2100550.

(10) Guo, L.; Gu, X.; Zhu, X.; Sun, X. Recent advances in molecular spintronics: Multifunctional spintronic devices. *Adv. Mater.* **2019**, *31*, 1805355.

(11) Ding, M.; Gu, X.; Guo, L.; Zhang, R.; Zhu, X.; Li, R.; Zhang, X.; Hu, W.; Sun, X. The prospects of organic semiconductor single crystals for spintronic applications. *J. Mater. Chem. C* **2022**,

(12) Privitera, A.; Righetto, M.; Cacialli, F.; Riede, M. K. Perspectives of Organic and Perovskite-Based Spintronics. *Adv. Opt. Mater.* **2021**, *9*, 2100215.

(13) Chen, H.; Zhang, W.; Li, M.; He, G.; Guo, X. Interface engineering in organic field-effect transistors: Principles, applications, and perspectives. *Chem. Rev.* **2020**, *120*, 2879–2949.

(14) Yuvaraja, S.; Nawaz, A.; Liu, Q.; Dubal, D.; Surya, S. G.; Salama, K. N.; Sonar, P. Organic field-effect transistor-based flexible sensors. *Chem. Soc. Rev.* **2020**, *49*, 3423–3460.

(15) Kim, M.; Ryu, S. U.; Park, S. A.; Choi, K.; Kim, T.; Chung, D.; Park, T. Donor–acceptor-conjugated polymer for high-performance organic field-effect transistors: a progress report. *Adv. Funct. Mat.* **2020**, *30*, 1904545.

(16) Shi, W.; Guo, Y.; Liu, Y. When flexible organic field-effect transistors meet biomimetics: a prospective view of the internet of things. *Adv. Mater.* **2020**, *32*, 1901493.

(17) Chow, P. C.; Someya, T. Organic photodetectors for next-generation wearable electronics. *Adv. Mater.* **2020**, *32*, 1902045.

(18) Li, Z.; Sinha, S. K.; Treich, G. M.; Wang, Y.; Yang, Q.; Deshmukh, A. A.; Sotzing, G. A.; Cao, Y. All-organic flexible fabric antenna for wearable electronics. *J. Mater. Chem. C* . **2020**, *8*, 5662–5667.

(19) Noh, J.; Kim, G.-U.; Han, S.; Oh, S. J.; Jeon, Y.; Jeong, D.; Kim, S. W.; Kim, T.-S.; Kim, B. J.; Lee, J.-Y. Intrinsically stretchable organic solar cells with efficiencies of over 11%. *ACS Energy Lett.* **2021**, *6*, 2512–2518.

(20) Liu, Y.-F.; Feng, J.; Bi, Y.-G.; Yin, D.; Sun, H.-B. Recent developments in flexible organic light-emitting devices. *Adv. Mater. Technol.* **2019**, *4*, 1800371.

(21) Ling, H.; Liu, S.; Zheng, Z.; Yan, F. Organic flexible electronics. *Small Methods* **2018**, *2*, 1800070.

(22) Su, R.; Park, S. H.; Ouyang, X.; Ahn, S. I.; McAlpine, M. C. 3D-printed flexible organic light-emitting diode displays. *Sci. Adv.* **2022**, *8*, eabl8798.

(23) Zhou, L.; Wanga, A.; Wu, S.-C.; Sun, J.; Park, S.; Jackson, T. N. All-organic active matrix flexible display. *Appl. Phys. Lett.* **2006**, *88*, 083502.

(24) Ji, D.; Li, T.; Hu, W.; Fuchs, H. Recent progress in aromatic polyimide dielectrics for organic electronic devices and circuits. *Adv. Mater.* **2019**, *31*, 1806070.

(25) Jang, J.; Song, Y.; Yoo, D.; Ober, C. K.; Lee, J.-K.; Lee, T. The development of fluorous photolithographic materials and their applications to achieve flexible organic electronic devices. *Flex. Print* **2016**, *1*, 023001.

(26) Torsi, L.; Magliulo, M.; Manoli, K.; Palazzo, G. Organic field-effect transistor sensors: a tutorial review. *Chem. Soc. Rev.* **2013**, *42*, 8612–8628.

(27) Jalal, A. H.; Alam, F.; Roychoudhury, S.; Umasankar, Y.; Pala, N.; Bhansali, S. Prospects and challenges of volatile organic compound sensors in human healthcare. *Acs Sens.* **2018**, *3*, 1246–1263.

(28) Cote, A. P.; Benin, A. I.; Ockwig, N. W.; O'Keeffe, M.; Matzger, A. J.; Yaghi, O. M. Porous, crystalline, covalent organic frameworks. *Science* **2005**, *310*, 1166–1170.

(29) Rodríguez-San-Miguel, D.; Zamora, F. Processing of covalent organic frameworks: an ingredient for a material to succeed. *Chem. Soc. Rev.* **2019**, *48*, 4375–4386.

(30) Chen, X.; Geng, K.; Liu, R.; Tan, K. T.; Gong, Y.; Li, Z.; Tao, S.; Jiang, Q.; Jiang, D. Covalent Organic Frameworks: Chemical Approaches to Designer Structures and Built-In Functions. *Angew. Chem. Int. Ed.* **2020**, *59*, 5050–5091.

(31) Geng, K.; He, T.; Liu, R.; Dalapati, S.; Tan, K. T.; Li, Z.; Tao, S.; Gong, Y.; Jiang, Q.; Jiang, D. Covalent organic frameworks: design, synthesis, and functions. *Chem. Rev.* **2020**, *120*, 8814–8933.

(32) Kandambeth, S.; Dey, K.; Banerjee, R. Covalent organic frameworks: chemistry beyond the structure. *J. Am. Chem. Soc.* **2018**, *141*, 1807–1822.

(33) Lohse, M. S.; Bein, T. Covalent organic frameworks: structures, synthesis, and applications. *Adv. Funct. Mater.* **2018**, *28*, 1705553.

(34) Dalapati, S.; Addicoat, M.; Jin, S.; Sakurai, T.; Gao, J.; Xu, H.; Irle, S.; Seki, S.; Jiang, D. Rational design of crystalline supermicroporous covalent organic frameworks with triangular topologies. *Nat. Commun.* **2015**, *6*, 1–8.

(35) Huang, N.; Wang, P.; Jiang, D. Covalent organic frameworks: a materials platform for structural and functional designs. *Nat. Rev. Mater.* **2016**, *1*, 1–19.

(36) Uribe-Romo, F. J.; Hunt, J. R.; Furukawa, H.; Klock, C.; O'Keeffe, M.; Yaghi, O. M. A crystalline imine-linked 3-D porous covalent organic framework. *J. Am. Chem. Soc.* **2009**, *131*, 4570–4571.

(37) Uribe-Romo, F. J.; Doonan, C. J.; Furukawa, H.; Oisaki, K.; Yaghi, O. M. Crystalline covalent organic frameworks with hydrazone linkages. *J. Am. Chem. Soc.* **2011**, *133*, 11478–11481.

(38) Segura, J. L.; Mancheño, M. J.; Zamora, F. Covalent organic frameworks based on Schiff-base chemistry: synthesis, properties and potential applications. *Chem. Soc. Rev.* **2016**, *45*, 5635–5671.

(39) El-Kaderi, H. M.; Hunt, J. R.; Mendoza-Cortés, J. L.; Côté, A. P.; Taylor, R. E.; O'Keeffe, M.; Yaghi, O. M. Designed synthesis of 3D covalent organic frameworks. *Science* **2007**, *316*, 268–272.

(40) Feng, X.; Ding, X.; Jiang, D. Covalent organic frameworks. *Chem. Soc. Rev.* **2012**, *41*, 6010–6022.

(41) Furukawa, H.; Yaghi, O. M. Storage of hydrogen, methane, and carbon dioxide in highly porous covalent organic frameworks for clean energy applications. *J. Am. Chem. Soc.* **2009**, *131*, 8875–8883.

(42) Jin, E.; Asada, M.; Xu, Q.; Dalapati, S.; Addicoat, M. A.; Brady, M. A.; Xu, H.; Nakamura, T.; Heine, T.; Chen, Q. et al. Two-dimensional sp2 carbon–conjugated covalent organic frameworks. *Science* **2017**, *357*, 673–676.

(43) Colson, J. W.; Dichtel, W. R. Rationally synthesized two-dimensional polymers. *Nat. Chem.* **2013**, *5*, 453–465.

(44) Bisbey, R. P.; Dichtel, W. R. Covalent organic frameworks as a platform for multidimensional polymerization. *ACS Cent. Sci.* **2017**, *3*, 533–543.

(45) Waller, P. J.; Gándara, F.; Yaghi, O. M. Chemistry of covalent organic frameworks. *Acc. Chem. Res.* **2015**, *48*, 3053–3063.

(46) Yazdani, H.; Shahbazi, M.-A.; Varma, R. S. 2D and 3D Covalent Organic Frameworks: Cutting-Edge Applications in Biomedical Sciences. *ACS Appl. Bio Mater.* **2021**, *5*, 40–58.

(47) Xia, R.; Zheng, X.; Li, C.; Yuan, X.; Wang, J.; Xie, Z.; Jing, X. Nanoscale Covalent Organic Frameworks with Donor–Acceptor Structure for Enhanced Photothermal Ablation of Tumors. *ACS nano* **2021**, *15*, 7638–7648.

(48) Wang, K.; Zhang, Z.; Lin, L.; Hao, K.; Chen, J.; Tian, H.; Chen, X. Cyanine-assisted exfoliation of covalent organic frameworks in nanocomposites for highly efficient chemo-photothermal tumor therapy. *ACS Appl. Mater. Interfaces* **2019**, *11*, 39503–39512.

(49) Mi, Z.; Yang, P.; Wang, R.; Unruangsri, J.; Yang, W.; Wang, C.; Guo, J. Stable radical

cation-containing covalent organic frameworks exhibiting remarkable structure-enhanced photothermal conversion. *J. Am. Chem. Soc.* **2019**, *141*, 14433–14442.

(50) Gao, P.; Wei, R.; Liu, X.; Chen, Y.; Wu, T.; Shi, M.; Wang, M.; Li, N.; Tang, B. Covalent organic framework-engineered polydopamine nanoplatform for multimodal imaging-guided tumor photothermal-chemotherapy. *ChemComm* **2021**, *57*, 5646–5649.

(51) Wang, B.; Liu, X.; Gong, P.; Ge, X.; Liu, Z.; You, J. Fluorescent COFs with a highly conjugated structure for visual drug loading and responsive release. *ChemComm* **2020**, *56*, 519–522.

(52) Scicluna, M. C.; Vella-Zarb, L. Evolution of nanocarrier drug-delivery systems and recent advancements in covalent organic framework–drug systems. *ACS Appl. Nano Mater.* **2020**, *3*, 3097–3115.

(53) Singh, N.; Son, S.; An, J.; Kim, I.; Choi, M.; Kong, N.; Tao, W.; Kim, J. S. Nanoscale porous organic polymers for drug delivery and advanced cancer theranostics. *Chem. Soc. Rev.* **2021**, *50*, 12883–12896.

(54) Fang, Q.; Wang, J.; Gu, S.; Kaspar, R. B.; Zhuang, Z.; Zheng, J.; Guo, H.; Qiu, S.; Yan, Y. 3D porous crystalline polyimide covalent organic frameworks for drug delivery. *J. Am. Chem. Soc.* **2015**, *137*, 8352–8355.

(55) Zhan, X.; Chen, Z.; Zhang, Q. Recent progress in two-dimensional COFs for energy-related applications. *J. Mater. Chem. A* **2017**, *5*, 14463–14479.

(56) Alahakoon, S. B.; Thompson, C. M.; Occhialini, G.; Smaldone, R. A. Design principles for covalent organic frameworks in energy storage applications. *ChemSusChem* **2017**, *10*, 2116–2129.

(57) Chang, F.; Zhou, J.; Chen, P.; Chen, Y.; Jia, H.; Saad, S. M.; Gao, Y.; Cao, X.; Zheng, T.

Microporous and mesoporous materials for gas storage and separation: a review. *Asia-Pac. J. Chem. Eng.* **2013**, *8*, 618–626.

(58) Li, Z.; Feng, X.; Zou, Y.; Zhang, Y.; Xia, H.; Liu, X.; Mu, Y. A 2D azine-linked covalent organic framework for gas storage applications. *ChemComm* **2014**, *50*, 13825–13828.

(59) Yang, Q.; Luo, M.; Liu, K.; Cao, H.; Yan, H. Covalent organic frameworks for photocatalytic applications. *Appl. Catal. B* **2020**, *276*, 119174.

(60) Wang, G.-B.; Li, S.; Yan, C.-X.; Zhu, F.-C.; Lin, Q.-Q.; Xie, K.-H.; Geng, Y.; Dong, Y.-B. Covalent organic frameworks: emerging high-performance platforms for efficient photocatalytic applications. *J. Mater. Chem. A* **2020**, *8*, 6957–6983.

(61) Yang, Y.; Zhang, P.; Hao, L.; Cheng, P.; Chen, Y.; Zhang, Z. Grotthuss proton-conductive covalent organic frameworks for efficient proton pseudocapacitors. *Angew. Chem. Int. Ed.* **2021**, *133*, 22009–22016.

(62) Guo, Z.-C.; You, M.-L.; Wang, Z.-J.; Li, Z.-F.; Li, G. Metal@ COFs Possess High Proton Conductivity with Mixed Conducting Mechanisms. *ACS Appl. Mater. Interfaces* **2022**, *14*, 15687–15696.

(63) Cai, S.-L.; Zhang, Y.-B.; Pun, A. B.; He, B.; Yang, J.; Toma, F. M.; Sharp, I. D.; Yaghi, O. M.; Fan, J.; Zheng, S.-R. et al. Tunable electrical conductivity in oriented thin films of tetrathiafulvalene-based covalent organic framework. *Chem. Sci.* **2014**, *5*, 4693–4700.

(64) Lakshmi, V.; Liu, C.-H.; Rajeswara Rao, M.; Chen, Y.; Fang, Y.; Dadvand, A.; Hamzehpoor, E.; Sakai-Otsuka, Y.; Stein, R. S.; Perepichka, D. F. A Two-Dimensional Poly (azatriangulene) Covalent Organic Framework with Semiconducting and Paramagnetic States. *J. Am. Chem. Soc.* **2020**, *142*, 2155–2160.

(65) Rotter, J. M.; Guntermann, R.; Auth, M.; Mähringer, A.; Sperlich, A.; Dyakonov, V.; Medina, D. D.; Bein, T. Highly conducting Wurster-type twisted covalent organic frameworks. *Chem. Sci.* **2020**, *11*, 12843–12853.

(66) Li, H.; Chang, J.; Li, S.; Guan, X.; Li, D.; Li, C.; Tang, L.; Xue, M.; Yan, Y.; Valtchev, V. et al. Three-dimensional tetrathiafulvalene-based covalent organic frameworks for tunable electrical conductivity. *J. Am. Chem. Soc.* **2019**, *141*, 13324–13329.

(67) Souto, M.; Perepichka, D. F. Electrically conductive covalent organic frameworks: bridging the fields of organic metals and 2D materials. *J. Mater. Chem. C* **2021**, *9*, 10668–10676.

(68) Wang, M.; Wang, M.; Lin, H.-H.; Ballabio, M.; Zhong, H.; Bonn, M.; Zhou, S.; Heine, T.; Canovas, E.; Dong, R. et al. High-mobility semiconducting two-dimensional conjugated covalent organic frameworks with p-type doping. *Journal of the American Chemical Society* **2020**, *142*, 21622–21627.

(69) Yue, Y.; Li, H.; Chen, H.; Huang, N. Piperazine-Linked Covalent Organic Frameworks with High Electrical Conductivity. *J. Am. Chem. Soc.* **2022**, *144*, 2873–2878.

(70) Xu, X.; Wang, S.; Yue, Y.; Huang, N. Semiconductive porphyrin-based covalent organic frameworks for sensitive near-infrared detection. *ACS Appl. Mater. Interfaces* **2020**, *12*, 37427–37434.

(71) Bian, G.; Yin, J.; Zhu, J. Recent advances on conductive 2D covalent organic frameworks. *Small* **2021**, *17*, 2006043.

(72) Friederich, P.; Fediai, A.; Kaiser, S.; Konrad, M.; Jung, N.; Wenzel, W. Toward design of novel materials for organic electronics. *Adv. Mater.* **2019**, *31*, 1808256.

(73) Chen, H.; Ginzburg, V. V.; Yang, J.; Yang, Y.; Liu, W.; Huang, Y.; Du, L.; Chen, B. Thermal conductivity of polymer-based composites: Fundamentals and applications. *Prog. Polym. Sci.* **2016**, *59*, 41–85.

(74) Huang, C.; Qian, X.; Yang, R. Thermal conductivity of polymers and polymer nanocomposites. *Mater. Sci. Eng.* **2018**, *132*, 1–22.

(75) Xu, X.; Chen, J.; Zhou, J.; Li, B. Thermal conductivity of polymers and their nanocomposites. *Adv. Mater.* **2018**, *30*, 1705544.

(76) Paulsen, B. D.; Tybrandt, K.; Stavrinidou, E.; Rivnay, J. Organic mixed ionic–electronic conductors. *Nat. Mater.* **2020**, *19*, 13–26.

(77) Lu, Y.; Yu, Z.-D.; Un, H.-I.; Yao, Z.-F.; You, H.-Y.; Jin, W.; Li, L.; Wang, Z.-Y.; Dong, B.-W.; Barlow, S. et al. Persistent Conjugated Backbone and Disordered Lamellar Packing Impart Polymers with Efficient n-Doping and High Conductivities. *Adv. Mater.* **2021**, *33*, 2005946.

(78) Jin, H.; Li, J.; Iocozzia, J.; Zeng, X.; Wei, P.-C.; Yang, C.; Li, N.; Liu, Z.; He, J. H.; Zhu, T. et al. Hybrid organic–inorganic thermoelectric materials and devices. *Angew. Chem. Int. Ed.* **2019**, *58*, 15206–15226.

(79) Kulkarni, S. A.; Yantara, N.; Tan, K. S.; Mathews, N.; Mhaisalkar, S. G. Perovskite nanostructures: leveraging quantum effects to challenge optoelectronic limits. *Mater.* **2020**, *33*, 122–140.

(80) Gao, Y.; Huang, C.; Hao, C.; Sun, S.; Zhang, L.; Zhang, C.; Duan, Z.; Wang, K.; Jin, Z.; Zhang, N. et al. Lead halide perovskite nanostructures for dynamic color display. *ACS nano* **2018**, *12*, 8847–8854.

(81) Liu, Y.; Cui, J.; Du, K.; Tian, H.; He, Z.; Zhou, Q.; Yang, Z.; Deng, Y.; Chen, D.; Zuo, X. et al. Efficient blue light-emitting diodes based on quantum-confined bromide perovskite nanostructures. *Nat. Photonics* **2019**, *13*, 760–764.

(82) Kojima, A.; Teshima, K.; Shirai, Y.; Miyasaka, T. Organometal halide perovskites as visible-light sensitizers for photovoltaic cells. *J. Am. Chem. Soc.* **2009**, *131*, 6050–6051.

(83) Yuan, M.; Quan, L. N.; Comin, R.; Walters, G.; Sabatini, R.; Voznyy, O.; Hoogland, S.; Zhao, Y.; Beauregard, E. M.; Kanjanaboos, P. et al. Perovskite energy funnels for efficient light-emitting diodes. *Nat. Nanotechnol.* **2016**, *11*, 872–877.

(84) Brenner, T. M.; Egger, D. A.; Kronik, L.; Hodes, G.; Cahen, D. Hybrid organic—inorganic perovskites: low-cost semiconductors with intriguing charge-transport properties. *Nat. Rev. Mater.* **2016**, *1*, 1–16.

(85) Yin, H.-Q.; Yin, X.-B. Metal–organic frameworks with multiple luminescence emissions: designs and applications. *Acc. Chem. Res.* **2020**, *53*, 485–495.

(86) Yang, J.; Yang, Y.-W. Metal–organic frameworks for biomedical applications. *Small* **2020**, *16*, 1906846.

(87) Xiao, X.; Zou, L.; Pang, H.; Xu, Q. Synthesis of micro/nanoscaled metal–organic frameworks and their direct electrochemical applications. *Chem. Soc. Rev.* **2020**, *49*, 301–331.

(88) Asha, K.; Bhattacharyya, K.; Mandal, S. Discriminative detection of nitro aromatic explosives by a luminescent metal–organic framework. *J. Mater. Chem. C* **2014**, *2*, 10073–10081.

(89) Chandra Rao, P.; Mandal, S. Europium-based metal–organic framework as a dual luminescence sensor for the selective detection of the phosphate anion and Fe3+ ion in aqueous media. *Inorg. Chem.* **2018**, *57*, 11855–11858.

(90) Mandal, S.; Natarajan, S.; Mani, P.; Pankajakshan, A. Post-Synthetic Modification of Metal–Organic Frameworks Toward Applications. *Adv. Funct. Mater,* **2021**, *31*, 2006291.

(91) Lu, M.; Zhang, Y.; Wang, S.; Guo, J.; Yu, W. W.; Rogach, A. L. Metal halide perovskite light-emitting devices: promising technology for next-generation displays. *Adv. Funct. Mater.* **2019**, *29*, 1902008.

(92) Li, Z.; Klein, T. R.; Kim, D. H.; Yang, M.; Berry, J. J.; Van Hest, M. F.; Zhu, K. Scalable fabrication of perovskite solar cells. *Nat. Rev. Mater.* **2018**, *3*, 1–20.

(93) Mahapatra, A.; Prochowicz, D.; Tavakoli, M. M.; Trivedi, S.; Kumar, P.; Yadav, P. A review of aspects of additive engineering in perovskite solar cells. *J. Mater. Chem. A* **2020**, *8*, 27–54.

(94) Rambabu, D.; Lakraychi, A. E.; Wang, J.; Sieuw, L.; Gupta, D.; Apostol, P.; Chanteux, G.; Goossens, T.; Robeyns, K.; Vlad, A. An Electrically Conducting Li-Ion Metal–Organic Framework. *J. Am. Chem. Soc.* **2021**, *143*, 11641–11650.

(95) Wu, X.; Qiu, Y.; Chen, Z.; Guan, B.; Hao, X.; Rykov, A. I.; Sun, Y.; Liu, L.; Zou, Y.; Sun, J. et al. Paramagnetic Conducting Metal–Organic Frameworks with Three-Dimensional Structure. *Angew. Chem. Int. Ed.* **2020**, *59*, 20873–20878.

(96) Sun, L.; Campbell, M. G.; Dincă, M. Electrically conductive porous metal–organic frameworks. *Angew. Chem. Int. Ed.* **2016**, *55*, 3566–3579.

(97) Xie, L. S.; Skorupskii, G.; Dincă, M. Electrically conductive metal–organic frameworks. *Chem. Rev.* **2020**, *120*, 8536–8580.

(98) Green, M. A.; Ho-Baillie, A.; Snaith, H. J. The emergence of perovskite solar cells. *Nat. photonics* **2014**, *8*, 506–514.

(99) Rong, Y.; Hu, Y.; Mei, A.; Tan, H.; Saidaminov, M. I.; Seok, S. I.; McGehee, M. D.; Sargent, E. H.; Han, H. Challenges for commercializing perovskite solar cells. *Science* **2018**, *361*, eaat8235.

(100) Sutherland, B. R.; Sargent, E. H. Perovskite photonic sources. *Nat. Photonics* **2016**, *10*, 295–302.

(101) Katan, C.; Mercier, N.; Even, J. Quantum and dielectric confinement effects in lower-dimensional hybrid perovskite semiconductors. *Chem. Rev.* **2019**, *119*, 3140–3192.

(102) Mao, L.; Stoumpos, C. C.; Kanatzidis, M. G. Two-dimensional hybrid halide perovskites: principles and promises. *J. Am. Chem. Soc.* **2018**, *141*, 1171–1190.

(103) Mancuso, J. L.; Mroz, A. M.; Le, K. N.; Hendon, C. H. Electronic structure modeling of metal–organic frameworks. *Chem. Rev.* **2020**, *120*, 8641–8715.

(104) Ni, X.; Li, H.; Liu, F.; Brédas, J.-L. Engineering of flat bands and Dirac bands in two-dimensional covalent organic frameworks (COFs): relationships among molecular orbital symmetry, lattice symmetry, and electronic-structure characteristics. *Mater. Horiz.* **2022**, *9*, 88–98.

(105) Thomas, S.; Li, H.; Zhong, C.; Matsumoto, M.; Dichtel, W. R.; Bredas, J.-L. Electronic structure of two-dimensional π-conjugated covalent organic frameworks. *Chem. Mater.* **2019**, *31*, 3051–3065.

(106) Joshi, T.; Chen, C.; Li, H.; Diercks, C. S.; Wang, G.; Waller, P. J.; Li, H.; Brédas, J.-L.; Yaghi, O. M.; Crommie, M. F. Local Electronic Structure of Molecular Heterojunctions in a Single-Layer 2D Covalent Organic Framework. *Adv. Mater.* **2019**, *31*, 1805941.

(107) Li, H.; Brédas, J.-L. Impact of structural defects on the elastic properties of two-dimensional covalent organic frameworks (2D COFs) under tensile stress. *Chem. Mater.* **2021**, *33*, 4529–4540.

(108) Li, H.; Li, H.; Xun, S.; Brédas, J.-L. Doping Modulation of the Charge Injection Barrier between a Covalent Organic Framework Monolayer and Graphene. *Chem. Mater.* **2020**, *32*, 9228–9237.

(109) Wang, S.; Chavez, A. D.; Thomas, S.; Li, H.; Flanders, N. C.; Sun, C.; Strauss, M. J.; Chen, L. X.; Markvoort, A. J.; Brédas, J.-L. et al. Pathway complexity in the stacking of imine-linked macrocycles related to two-dimensional covalent organic frameworks. *Chem. Mater.* **2019**, *31*, 7104–7111.

(110) Borboudakis, G.; Stergiannakos, T.; Frysali, M.; Klontzas, E.; Tsamardinos, I.; Froudakis, G. E. Chemically intuited, large-scale screening of MOFs by machine learning techniques. *Npj Comput. Mater.* **2017**, *3*, 1–7.

(111) Anderson, R.; Rodgers, J.; Argueta, E.; Biong, A.; Gómez-Gualdrón, D. A. Role of pore chemistry and topology in the CO2 capture capabilities of MOFs: from molecular simulation to machine learning. *Chem. Mater.* **2018**, *30*, 6325–6337.

(112) Fabrizio, K.; Le, K. N.; Andreeva, A. B.; Hendon, C. H.; Brozek, C. K. Determining Optical Band Gaps of MOFs. *ACS Mater. Lett.* **2022**, *4*, 457–463.

(113) Chong, S.; Lee, S.; Kim, B.; Kim, J. Applications of machine learning in metal-organic frameworks. *Coord. Chem. Rev.* **2020**, *423*, 213487.

(114) Shi, Z.; Yang, W.; Deng, X.; Cai, C.; Yan, Y.; Liang, H.; Liu, Z.; Qiao, Z. Machine-learning-assisted high-throughput computational screening of high performance metal–organic frameworks. *Mol. Syst. Des. Eng.* **2020**, *5*, 725–742.

(115) Nandy, A.; Duan, C.; Kulik, H. J. Using Machine Learning and Data Mining to Leverage Community Knowledge for the Engineering of Stable Metal–Organic Frameworks. *J. Am. Chem. Soc.* **2021**, *143*, 17535–17547.

(116) Tao, Q.; Xu, P.; Li, M.; Lu, W. Machine learning for perovskite materials design and discovery. *Npj Comput. Mater.* **2021**, *7*, 1–18.

(117) Lyu, R.; Moore, C. E.; Liu, T.; Yu, Y.; Wu, Y. Predictive Design Model for Low-Dimensional Organic–Inorganic Halide Perovskites Assisted by Machine Learning. *J. Am. Chem. Soc.* **2021**, *143*, 12766–12776.

(118) Talapatra, A.; Uberuaga, B. P.; Stanek, C. R.; Pilania, G. A machine learning approach for the prediction of formability and thermodynamic stability of single and double perovskite oxides. *Chem. Mater.* **2021**, *33*, 845–858.

(119) Kim, J.; Kang, D.; Kim, S.; Jang, H. W. Catalyze materials science with machine learning. *ACS Mater. Lett.* **2021**, *3*, 1151–1171.

(120) Rosen, A. S.; Notestein, J. M.; Snurr, R. Q. Realizing the data-driven, computational discovery of metal-organic framework catalysts. *Curr. Opin. Chem. Eng.* **2022**, *35*, 100760.

(121) McCarver, G. A.; Rajeshkumar, T.; Vogiatzis, K. D. Computational catalysis for metal-organic frameworks: An overview. *Coord. Chem. Rev.* **2021**, *436*, 213777.

(122) Kitchin, J. R. Machine learning in catalysis. *Nat. Catal.* **2018**, *1*, 230–232.

(123) Hwang, J.; Rao, R. R.; Giordano, L.; Katayama, Y.; Yu, Y.; Shao-Horn, Y. Perovskites in catalysis and electrocatalysis. *Science* **2017**, *358*, 751–756.

(124) Altintas, C.; Altundal, O. F.; Keskin, S.; Yildirim, R. Machine learning meets with metal organic frameworks for gas storage and separation. *J. Chem. Inf. Model* **2021**, *61*, 2131–2146.

(125) Gladkikh, V.; Kim, D. Y.; Hajibabaei, A.; Jana, A.; Myung, C. W.; Kim, K. S. Machine learning for predicting the band gaps of ABX3 perovskites from elemental properties. *J. Phys. Chem. C* **2020**, *124*, 8905–8918.

(126) Mayr, F.; Harth, M.; Kouroudis, I.; Rinderle, M.; Gagliardi, A. Machine Learning and Optoelectronic Materials Discovery: A Growing Synergy. *J. Phys. Chem. Lett.* **2022**, *13*, 1940–1951.

(127) Chen, C.; Zuo, Y.; Ye, W.; Li, X.; Deng, Z.; Ong, S. P. A critical review of machine learning of energy materials. *Adv. Energy Mater.* **2020**, *10*, 1903242.

(128) Li, J.; Pradhan, B.; Gaur, S.; Thomas, J. Predictions and strategies learned from machine learning to develop high-performing perovskite solar cells. *Adv. Energy Mater.* **2019**, *9*, 1901891.

(129) Baranowski, M.; Plochocka, P. Excitons in metal-halide perovskites. *Adv. Energy Mater.* **2020**, *10*, 1903659.

(130) Blancon, J.-C.; Stier, A. V.; Tsai, H.; Nie, W.; Stoumpos, C. C.; Traore, B.; Pedesseau, L.; Kepenekian, M.; Katsutani, F.; Noe, G. et al. Scaling law for excitons in 2D perovskite quantum wells. *Nat. Commun.* **2018**, *9*, 1–10.

(131) Dyksik, M.; Duim, H.; Maude, D. K.; Baranowski, M.; Loi, M. A.; Plochocka, P. Brightening of dark excitons in 2D perovskites. *Sci. Adv.* **2021**, *7*, eabk0904.

(132) Proppe, A. H.; Elkins, M. H.; Voznyy, O.; Pensack, R. D.; Zapata, F.; Besteiro, L. V.; Quan, L. N.; Quintero-Bermudez, R.; Todorovic, P.; Kelley, S. O. et al. Spectrally resolved ultrafast exciton transfer in mixed perovskite quantum wells. *J. Phys. Chem. Lett.* **2019**, *10*, 419–426.

(133) Rajasree, S. S.; Yu, J.; Pratik, S. M.; Li, X.; Wang, R.; Kumbhar, A. S.; Goswami, S.; Cramer, C. J.; Deria, P. Superradiance and Directional Exciton Migration in Metal–Organic Frameworks. *J. Am. Chem. Soc.* **2022**, *144*, 1396–1406.

(134) Cao, L.; Lin, Z.; Shi, W.; Wang, Z.; Zhang, C.; Hu, X.; Wang, C.; Lin, W. Exciton migration and amplified quenching on two-dimensional metal–organic layers. *J. Am. Chem. Soc.* **2017**, *139*, 7020–7029.

(135) Yu, J.; Anderson, R.; Li, X.; Xu, W.; Goswami, S.; Rajasree, S. S.; Maindan, K.; Gómez-Gualdrón, D. A.; Deria, P. Improving Energy Transfer within Metal–Organic Frameworks by Aligning Linker Transition Dipoles along the Framework Axis. *J. Am. Chem. Soc.* **2020**, *142*, 11192–11202.

(136) Mahato, P.; Monguzzi, A.; Yanai, N.; Yamada, T.; Kimizuka, N. Fast and long-range triplet exciton diffusion in metal–organic frameworks for photon upconversion at ultralow excitation power. *Nat. Mater.* **2015**, *14*, 924–930.

(137) Sample, A. D.; Guan, J.; Hu, J.; Reese, T.; Cherqui, C. R.; Park, J.-E.; Freire-Fernández, F.; Schaller, R. D.; Schatz, G. C.; Odom, T. W. Strong coupling between plasmons and molecular excitons in metal–organic frameworks. *Nano Lett.* **2021**, *21*, 7775–7780.

(138) Son, H.-J.; Jin, S.; Patwardhan, S.; Wezenberg, S. J.; Jeong, N. C.; So, M.; Wilmer, C. E.; Sarjeant, A. A.; Schatz, G. C.; Snurr, R. Q. et al. Light-harvesting and ultrafast energy migration in porphyrin-based metal–organic frameworks. *J. Am. Chem. Soc.* **2013**, *135*, 862–869.

(139) Zhang, Q.; Zhang, C.; Cao, L.; Wang, Z.; An, B.; Lin, Z.; Huang, R.; Zhang, Z.; Wang, C.; Lin, W. Förster Energy Transport in Metal–Organic Frameworks Is Beyond Step-by-Step Hopping. *J. Am. Chem. Soc.* **2016**, *138*, 5308–5315.

(140) Flanders, N. C.; Kirschner, M. S.; Kim, P.; Fauvell, T. J.; Evans, A. M.; Helweh, W.; Spencer, A. P.; Schaller, R. D.; Dichtel, W. R.; Chen, L. X. Large Exciton Diffusion Coefficients in Two-Dimensional Covalent Organic Frameworks with Different Domain Sizes Revealed by Ultrafast Exciton Dynamics. *J. Am. Chem. Soc.* **2020**, *142*, 14957–14965.

(141) Yang, S.; Streater, D.; Fiankor, C.; Zhang, J.; Huang, J. Conjugation-and aggregation-directed design of covalent organic frameworks as white-light-emitting diodes. *J. Am. Chem. Soc.* **2021**, *143*, 1061–1068.

(142) Yin, J.; Li, H.; Cortecchia, D.; Soci, C.; Brédas, J.-L. Excitonic and polaronic properties of 2D hybrid organic–inorganic perovskites. *ACS Energy Lett.* **2017**, *2*, 417–423.

(143) Zhao, L.; Lin, Y. L.; Kim, H.; Giebink, N. C.; Rand, B. P. Donor/acceptor charge-transfer states at two-dimensional metal halide perovskite and organic semiconductor interfaces. *ACS Energy Lett.* **2018**, *3*, 2708–2712.

(144) Keller, N.; Bein, T. Optoelectronic processes in covalent organic frameworks. *Chem. Soc. Rev.* **2021**, *50*, 1813–1845.

(145) Hestand, N. J.; Spano, F. C. Molecular aggregate photophysics beyond the Kasha model: novel design principles for organic materials. *Acc. Chem. Res.* **2017**, *50*, 341–350.

(146) Spano, F. C. The spectral signatures of Frenkel polarons in H-and J-aggregates. *Acc. Chem. Res.* **2010**, *43*, 429–439.

(147) Spano, F. C. Excitons in conjugated oligomer aggregates, films, and crystals. *Annu. Rev. Phys. Chem.* **2006**, *57*, 217–243.

(148) Wright, A. D.; Verdi, C.; Milot, R. L.; Eperon, G. E.; Pérez-Osorio, M. A.; Snaith, H. J.; Giustino, F.; Johnston, M. B.; Herz, L. M. Electron–phonon coupling in hybrid lead halide perovskites. *Nat. Commun.* **2016**, *7*, 1–9.

(149) Song, X.; Peng, C.; Xu, X.; Yin, J.; Fei, H. Efficient, broadband self-trapped white-light emission from haloplumbate-based metal–organic frameworks. *ChemComm* **2020**, *56*, 10078–10081.

(150) Zhang, G.; Yin, J.; Song, X.; Fei, H. A moisture-stable organosulfonate-based metal–organic framework with intrinsic self-trapped white-light emission. *ChemComm* **2020**, *56*, 1325–1328.

(151) Peng, C.; Song, X.; Yin, J.; Zhang, G.; Fei, H. Intrinsic White-Light-Emitting Metal–Organic Frameworks with Structurally Deformable Secondary Building Units. *Angew. Chem. Int. Ed.* **2019**, *131*, 7900–7904.

(152) Straus, D. B.; Hurtado Parra, S.; Iotov, N.; Gebhardt, J.; Rappe, A. M.; Subotnik, J. E.; Kikkawa, J. M.; Kagan, C. R. Direct observation of electron–phonon coupling and slow vibrational relaxation in organic–inorganic hybrid perovskites. *J. Am. Chem. Soc.* **2016**, *138*, 13798–13801.

(153) Straus, D. B.; Hurtado Parra, S.; Iotov, N.; Zhao, Q.; Gau, M. R.; Carroll, P. J.; Kikkawa, J. M.; Kagan, C. R. Tailoring hot exciton dynamics in 2D hybrid perovskites through cation modification. *ACS nano* **2020**, *14*, 3621–3629.

(154) McCall, K. M.; Stoumpos, C. C.; Kostina, S. S.; Kanatzidis, M. G.; Wessels, B. W. Strong electron–phonon coupling and self-trapped excitons in the defect halide perovskites A3M2I9 (A= Cs, Rb; M= Bi, Sb). *Chem. Mater.* **2017**, *29*, 4129–4145.

(155) Schultz, J. D.; Shin, J. Y.; Chen, M.; O'Connor, J. P.; Young, R. M.; Ratner, M. A.; Wasielewski, M. R. Influence of vibronic coupling on ultrafast singlet fission in a linear terrylenediimide dimer. *J. Am. Chem. Soc.* **2021**, *143*, 2049–2058.

(156) Lin, C.; Kim, T.; Schultz, J. D.; Young, R. M.; Wasielewski, M. R. Accelerating symmetry-breaking charge separation in a perylenediimide trimer through a vibronically coherent dimer intermediate. *Nat. Chem.* **2022**, 1–8.

(157) Tempelaar, R.; Reichman, D. R. Vibronic exciton theory of singlet fission. I. Linear absorption and the anatomy of the correlated triplet pair state. *J. Chem. Phys.* **2017**, *146*, 174703.

(158) Tempelaar, R.; Reichman, D. R. Vibronic exciton theory of singlet fission. II. Two-dimensional spectroscopic detection of the correlated triplet pair state. *J. Chem. Phys.* **2017**, *146*, 174704.

(159) Tempelaar, R.; Reichman, D. R. Vibronic exciton theory of singlet fission. III. How vibronic coupling and thermodynamics promote rapid triplet generation in pentacene crystals. *J. Chem. Phys.* **2018**, *148*, 244701.

(160) Miyata, K.; Conrad-Burton, F. S.; Geyer, F. L.; Zhu, X.-Y. Triplet pair states in singlet fission. *Chem. Rev.* **2019**, *119*, 4261–4292.

(161) Arsenault, E. A.; Schile, A. J.; Limmer, D. T.; Fleming, G. R. Vibronic coupling in energy transfer dynamics and two-dimensional electronic–vibrational spectra. *J. Chem. Phys.* **2021**, *155*, 054201.

(162) Arsenault, E. A.; Bhattacharyya, P.; Yoneda, Y.; Fleming, G. R. Two-dimensional electronic–vibrational spectroscopy: Exploring the interplay of electrons and nuclei in excited state molecular dynamics. *J. Chem. Phys.* **2021**, *155*, 020901.

(163) Scholes, G. D.; Fleming, G. R. On the mechanism of light harvesting in photosynthetic purple bacteria: B800 to B850 energy transfer. *J. Phys. Chem. B* **2000**, *104*, 1854–1868.

(164) Blase, X.; Duchemin, I.; Jacquemin, D. The Bethe–Salpeter equation in chemistry: relations with TD-DFT, applications and challenges. *Chem. Soc. Rev.* **2018**, *47*, 1022–1043.

(165) Blase, X.; Duchemin, I.; Jacquemin, D.; Loos, P.-F. The Bethe–Salpeter equation formalism: From physics to chemistry. *J. Phys. Chem. Lett.* **2020**, *11*, 7371–7382.

(166) Bradbury, N.; Nguyen, M.; Caram, J. R.; Neuhauser, D. Bethe Salpeter Equation Spectra for Very Large Systems. *arXiv preprint arXiv:2205.06690* **2022**,

(167) Ortega-Guerrero, A.; Fumanal, M.; Capano, G.; Smit, B. From isolated porphyrin ligands to periodic Al-PMOF: A comparative study of the optical properties using DFT/TDDFT. *J. Phys. Chem. B* **2020**, *124*, 21751–21760.

(168) Ji, M.; Lan, X.; Han, Z.; Hao, C.; Qiu, J. Luminescent properties of metal–organic framework MOF-5: relativistic time-dependent density functional theory investigations. *Inorg. Chem.* **2012**, *51*, 12389–12394.

(169) Wilbraham, L.; Coudert, F.-X.; Ciofini, I. Modelling photophysical properties of metal–organic frameworks: a density functional theory based approach. *Phys. Chem. Chem. Phys.* **2016**, *18*, 25176–25182.

(170) Kshirsagar, A. R.; Attaccalite, C.; Blase, X.; Li, J.; Poloni, R. Bethe–Salpeter Study of the Optical Absorption of trans and cis Azobenzene-Functionalized Metal–Organic Frameworks Using Molecular and Periodic Models. *The Journal of Physical Chemistry C* **2021**, *125*, 7401–7412.

(171) Kshirsagar, A. R.; Blase, X.; Attaccalite, C.; Poloni, R. Strongly Bound Excitons in Metal–Organic Framework MOF-5: A Many-Body Perturbation Theory Study. *J. Phys. Chem. Lett.* **2021**, *12*, 4045–4051.

(172) Hussain, M.; Song, X.; Zhao, J.; Luo, Y.; Hao, C. Impact of electronically excited state

hydrogen bonding on luminescent covalent organic framework: a TD-DFT investigation. *Mol. Phys.* **2019**, *117*, 823–830.

(173) Feng, T.; Streater, D.; Sun, B.; Duisenova, K.; Wang, D.; Liu, Y.; Huang, J.; Zhang, J. Tuning Photoexcited Charge Transfer in Imine-Linked Two-Dimensional Covalent Organic Frameworks. *J. Phys. Chem. Lett.* **2022**, *13*, 1398–1405.

(174) Sun, S.; Ma, H.-z.; Zhang, X.; Ma, Y.-c. Direct and indirect excitons in two-dimensional covalent organic frameworks. *Chinese J. Chem. Phys.* **2020**, *33*, 569–577.

(175) Molina-Sánchez, A. Excitonic states in semiconducting two-dimensional perovskites. *ACS Appl. Energy Mater.* **2018**, *1*, 6361–6367.

(176) Leveillee, J.; Katan, C.; Zhou, L.; Mohite, A. D.; Even, J.; Tretiak, S.; Schleife, A.; Neukirch, A. J. Influence of π-conjugated cations and halogen substitution on the optoelectronic and excitonic properties of layered hybrid perovskites. *Physical Review Materials* **2018**, *2*, 105406.

(177) Zhu, X.; Su, H.; Marcus, R. A.; Michel-Beyerle, M. E. Computed and experimental absorption spectra of the perovskite CH3NH3PbI3. *J. Phys. Chem. Lett.* **2014**, *5*, 3061–3065.

(178) Giorgi, G.; Yamashita, K.; Palummo, M. Nature of the electronic and optical excitations of Ruddlesden–Popper hybrid organic–inorganic perovskites: The role of the many-body interactions. *J. Phys. Chem. Lett.* **2018**, *9*, 5891–5896.

(179) Quarti, C.; Marchal, N.; Beljonne, D. Tuning the optoelectronic properties of two-dimensional hybrid perovskite semiconductors with alkyl chain spacers. *J. Phys. Chem. Lett.* **2018**, *9*, 3416–3424.

(180) Cho, Y.; Berkelbach, T. C. Optical properties of layered hybrid organic–inorganic halide perovskites: A tight-binding GW-BSE study. *J. Phys. Chem. Lett.* **2019**, *10*, 6189–6196.

(181) Zhang, Z.; Fang, W.-H.; Tokina, M. V.; Long, R.; Prezhdo, O. V. Rapid decoherence suppresses charge recombination in multi-layer 2D halide perovskites: Time-domain ab initio analysis. *Nano Lett.* **2018**, *18*, 2459–2466.

(182) Smith, M. D.; Pedesseau, L.; Kepenekian, M.; Smith, I. C.; Katan, C.; Even, J.; Karunadasa, H. I. Decreasing the electronic confinement in layered perovskites through intercalation. *Chem. Sci.* **2017**, *8*, 1960–1968.

(183) Monserrat, B. Electron–phonon coupling from finite differences. *J. Condens. Matter Phys.* **2018**, *30*, 083001.

(184) Nelson, T.; Fernandez-Alberti, S.; Roitberg, A. E.; Tretiak, S. Nonadiabatic excited-state molecular dynamics: Modeling photophysics in organic conjugated materials. *Acc. Chem. Res.* **2014**, *47*, 1155–1164.

(185) Nelson, T. R.; White, A. J.; Bjorgaard, J. A.; Sifain, A. E.; Zhang, Y.; Nebgen, B.; Fernandez-Alberti, S.; Mozyrsky, D.; Roitberg, A. E.; Tretiak, S. Non-adiabatic excited-state molecular dynamics: Theory and applications for modeling photophysics in extended molecular materials. *Chem. Rev.* **2020**, *120*, 2215–2287.

(186) Li, W.; She, Y.; Vasenko, A. S.; Prezhdo, O. V. Ab initio nonadiabatic molecular dynamics of charge carriers in metal halide perovskites. *Nanoscale* **2021**, *13*, 10239–10265.

(187) Ollitrault, P. J.; Mazzola, G.; Tavernelli, I. Nonadiabatic molecular quantum dynamics with quantum computers. *Phys. Rev. Lett.* **2020**, *125*, 260511.

(188) Mac Kernan, D.; Ciccotti, G.; Kapral, R. Trotter-based simulation of quantum-classical dynamics. *J. Phys. Chem. B* **2008**, *112*, 424–432.

(189) Barbatti, M. Nonadiabatic dynamics with trajectory surface hopping method. *Wiley Interdiscip. Rev. Comput. Mol. Sci.* **2011**, *1*, 620–633.

(190) Drude, P. Zur elektronentheorie der metalle. *Ann. Phys.* **1900**, *306*, 566–613.

(191) Drude, P. Zur elektronentheorie der metalle; II. Teil. galvanomagnetische und thermomagnetische effecte. *Ann. Phys.* **1900**, *308*, 369–402.

(192) Sommerfeld, A. On the electron theory of metals based on Fermian statistics. *journal for physics* **1928**, *47*, 1–32.

(193) Hubbard, J. Electron correlations in narrow energy bands. *Proc. R. Soc. London, Ser. A* **1963**, *276*, 238–257.

(194) Heisenberg, W. *Original Scientific Papers Wissenschaftliche Originalarbeiten*; Springer, 1985; pp 580–597.

(195) Holstein, T. Studies of polaron motion: Part I. The molecular-crystal model. *Ann. Phys.* **1959**, *8*, 325–342.

(196) Holstein, T. Studies of polaron motion: Part II. The "small" polaron. *Ann. Phys.* **1959**, *8*, 343–389.

(197) Kováčik, R.; Murthy, S. S.; Quiroga, C. E.; Ederer, C.; Franchini, C. Combined first-principles and model Hamiltonian study of the perovskite series R MnO 3 (R= La, Pr, Nd, Sm, Eu, and Gd). *Phys. Rev. B* **2016**, *93*, 075139.

(198) Jiang, W.; Ni, X.; Liu, F. Exotic topological bands and quantum states in metal–organic and covalent–organic frameworks. *Acc. Chem. Res.* **2021**, *54*, 416–426.

(199) Cui, B.; Zheng, X.; Wang, J.; Liu, D.; Xie, S.; Huang, B. Realization of Lieb lattice in covalent-organic frameworks with tunable topology and magnetism. *Nat. Commun.* **2020**, *11*, 1–8.

(200) Jiang, W.; Zhang, S.; Wang, Z.; Liu, F.; Low, T. Topological band engineering of Lieb lattice in Phthalocyanine-based metal–organic frameworks. *Nano Lett.* **2020**, *20*, 1959–1966.

(201) Chen, H.; Zhang, S.; Jiang, W.; Zhang, C.; Guo, H.; Liu, Z.; Wang, Z.; Liu, F.; Niu, X. Prediction of two-dimensional nodal-line semimetals in a carbon nitride covalent network. *J. Mater. Chem. A* **2018**, *6*, 11252–11259.

(202) Tanimura, Y. Stochastic Liouville, Langevin, Fokker–Planck, and master equation approaches to quantum dissipative systems. *J. Phys. Soc. Japan* **2006**, *75*, 082001.

(203) Ishizaki, A.; Fleming, G. R. On the adequacy of the Redfield equation and related approaches to the study of quantum dynamics in electronic energy transfer. *J. Chem. Phys.* **2009**, *130*, 234110.

(204) Kloss, B.; Reichman, D. R.; Tempelaar, R. Multiset matrix product state calculations reveal mobile Franck-Condon excitations under strong Holstein-type coupling. *Phys. Rev. Lett.* **2019**, *123*, 126601.

(205) Dunn, I. S.; Tempelaar, R.; Reichman, D. R. Removing instabilities in the hierarchical equations of motion: Exact and approximate projection approaches. *J. Chem. Phys.* **2019**, *150*, 184109.

(206) Philpott, M. R. Theory of the coupling of electronic and vibrational excitations in molecular crystals and helical polymers. *J. Chem. Phys.* **1971**, *55*, 2039–2054.

(207) Spano, F. C. Modeling disorder in polymer aggregates: The optical spectroscopy of regioregular poly (3-hexylthiophene) thin films. *J. Chem. Phys.* **2005**, *122*, 234701.

(208) Spano, F. C. Absorption and emission in oligo-phenylene vinylene nanoaggregates: The role of disorder and structural defects. *J. Chem. Phys.* **2002**, *116*, 5877–5891.

(209) Spano, F. C. The fundamental photophysics of conjugated oligomer herringbone aggregates. *J. Chem. Phys.* **2003**, *118*, 981–994.

(210) Stradomska, A.; Petelenz, P. Intermediate vibronic coupling in sexithiophene single crystals. *J. Chem. Phys.* **2009**, *130*, 094705.

(211) Stradomska, A.; Petelenz, P. Intermediate vibronic coupling in sexithiophene single crystals. II. Three-particle contributions. *J. Chem. Phys.* **2009**, *131*, 044507.

(212) Hoffmann, M.; Soos, Z. Optical absorption spectra of the Holstein molecular crystal for weak and intermediate electronic coupling. *Phys. Rev. B* **2002**, *66*, 024305.

(213) Scherer, P.; Fischer, S. F. On the theory of vibronic structure of linear aggregates. Application to pseudoisocyanin (PIC). *Chem. Phys.* **1984**, *86*, 269–283.

(214) Roden, J.; Eisfeld, A.; Briggs, J. S. The J-and H-bands of dye aggregate spectra: Analysis of the coherent exciton scattering (CES) approximation. *Chem. Phys.* **2008**, *352*, 258–266.

(215) Dell'Angelo, D.; Momeni, M. R.; Pearson, S.; Shakib, F. A. Modeling energy transfer and absorption spectra in layered metal–organic frameworks based on a Frenkel–Holstein Hamiltonian. *J. Chem. Phys.* **2022**, *156*, 044109.

(216) Ghosh, R.; Paesani, F. Unraveling the effect of defects, domain size, and chemical doping on photophysics and charge transport in covalent organic frameworks. *Chem. Sci.* **2021**, *12*, 8373–8384.

(217) Ghosh, R.; Paesani, F. Topology-Mediated Enhanced Polaron Coherence in Covalent Organic Frameworks. *J. Phys. Chem. Lett.* **2021**, *12*, 9442–9448.

(218) Gisslén, L.; Scholz, R. Crystallochromy of perylene pigments: Interference between Frenkel excitons and charge-transfer states. *Phys. Rev. B* **2009**, *80*, 115309.

(219) Hestand, N. J.; Spano, F. C. Expanded theory of H-and J-molecular aggregates: the effects of vibronic coupling and intermolecular charge transfer. *Chem. Rev.* **2018**, *118*, 7069–7163.

(220) Ghosh, R.; Pochas, C. M.; Spano, F. C. Polaron delocalization in conjugated polymer films. *J. Phys. Chem. C* **2016**, *120*, 11394–11406.

(221) Ghosh, R.; Chew, A. R.; Onorato, J.; Pakhnyuk, V.; Luscombe, C. K.; Salleo, A.; Spano, F. C. Spectral signatures and spatial coherence of bound and unbound polarons in p3ht films: Theory versus experiment. *J. Phys. Chem. C* **2018**, *122*, 18048–18060.

(222) Ghosh, R.; Luscombe, C. K.; Hambsch, M.; Mannsfeld, S. C.; Salleo, A.; Spano, F. C. Anisotropic polaron delocalization in conjugated homopolymers and donor–acceptor copolymers. *Chem. Mater.* **2019**, *31*, 7033–7045.

(223) Chew, A. R.; Ghosh, R.; Shang, Z.; Spano, F. C.; Salleo, A. Sequential doping reveals the importance of amorphous chain rigidity in charge transport of semi-crystalline polymers. *J. Phys. Chem. Lett.* **2017**, *8*, 4974–4980.

(224) Chew, A. R.; Ghosh, R.; Pakhnyuk, V.; Onorato, J.; Davidson, E. C.; Segalman, R. A.; Luscombe, C. K.; Spano, F. C.; Salleo, A. Unraveling the effect of conformational and electronic disorder in the charge transport processes of semiconducting polymers. *Adv. Funct. Mater.* **2018**, *28*, 1804142.

(225) Pochas, C. M.; Spano, F. C. New insights on the nature of two-dimensional polarons in semiconducting polymers: Infrared absorption in poly (3-hexylthiophene). *J. Chem. Phys.* **2014**, *140*, 244902.

(226) Clark, J.; Silva, C.; Friend, R. H.; Spano, F. C. Role of intermolecular coupling in the photophysics of disordered organic semiconductors: aggregate emission in regioregular polythiophene. *Phys. Rev. Lett.* **2007**, *98*, 206406.

(227) Niles, E. T.; Roehling, J. D.; Yamagata, H.; Wise, A. J.; Spano, F. C.; Moulé, A. J.; Grey, J. K. J-aggregate behavior in poly-3-hexylthiophene nanofibers. *J. Phys. Chem. Lett.* **2012**, *3*, 259–263.

(228) De Sio, A.; Troiani, F.; Maiuri, M.; Réhault, J.; Sommer, E.; Lim, J.; Huelga, S. F.; Plenio, M. B.; Rozzi, C. A.; Cerullo, G. et al. Tracking the coherent generation of polaron pairs in conjugated polymers. *Nat. Commun.* **2016**, *7*, 1–8.

(229) Barford, W.; Marcus, M. Perspective: Optical spectroscopy in π-conjugated polymers and how it can be used to determine multiscale polymer structures. *The Journal of Chemical Physics* **2017**, *146*, 130902.

(230) Marcus, M.; Milward, J. D.; Köhler, A.; Barford, W. Structural information for conjugated polymers from optical modeling. *J. Phys. Chem. A* **2018**, *122*, 3621–3625.

(231) Paquin, F.; Yamagata, H.; Hestand, N. J.; Sakowicz, M.; Bérubé, N.; Côté, M.; Reynolds, L. X.; Haque, S. A.; Stingelin, N.; Spano, F. C. et al. Two-dimensional spatial coherence of excitons in semicrystalline polymeric semiconductors: Effect of molecular weight. *Phys. Rev. B* **2013**, *88*, 155202.

(232) Milward, J. D.; Marcus, M.; Köhler, A.; Barford, W. Extracting structural information from MEH-PPV optical spectra. *J. Chem. Phys.* **2018**, *149*, 044903.

(233) Dunlap-Shohl, W. A.; Barraza, E. T.; Barrette, A.; Dovletgeldi, S.; Findik, G.; Dirkes, D. J.; Liu, C.; Jana, M. K.; Blum, V.; You, W. et al. Tunable internal quantum well alignment in rationally designed oligomer-based perovskite films deposited by resonant infrared matrix-assisted pulsed laser evaporation. *Mater. Horiz.* **2019**, *6*, 1707–1716.

(234) Straus, D. B.; Kagan, C. R. Electrons, excitons, and phonons in two-dimensional hybrid perovskites: connecting structural, optical, and electronic properties. *J. Phys. Chem. Lett.* **2018**, *9*, 1434–1447.

(235) Srimath Kandada, A. R.; Silva, C. Exciton polarons in two-dimensional hybrid metal-halide perovskites. *J. Phys. Chem. Lett.* **2020**, *11*, 3173–3184.

(236) Neutzner, S.; Thouin, F.; Cortecchia, D.; Petrozza, A.; Silva, C.; Kandada, A. R. S. Exciton-polaron spectral structures in two-dimensional hybrid lead-halide perovskites. *Phy. Rev. Mater.* **2018**, *2*, 064605.

(237) Haug, W. K.; Moscarello, E. M.; Wolfson, E. R.; McGrier, P. L. The luminescent and photophysical properties of covalent organic frameworks. *Chem. Soc. Rev.* **2020**, *49*, 839–864.

(238) Rice, A. M.; Martin, C. R.; Galitskiy, V. A.; Berseneva, A. A.; Leith, G. A.; Shustova, N. B. Photophysics modulation in photoswitchable metal–organic frameworks. *Chem. Rev.* **2019**, *120*, 8790–8813.

(239) Xu, S.; Zhang, Q. Recent progress in covalent organic frameworks as light-emitting materials. *Mater. Today Energy* **2021**, *20*, 100635.

(240) Banerjee, T.; Podjaski, F.; Kröger, J.; Biswal, B. P.; Lotsch, B. V. Polymer photocatalysts for solar-to-chemical energy conversion. *Nat. Rev. Mater.* **2021**, *6*, 168–190.

(241) Dolgopolova, E. A.; Rice, A. M.; Martin, C. R.; Shustova, N. B. Photochemistry and photophysics of MOFs: steps towards MOF-based sensing enhancements. *Chem. Soc. Rev.* **2018**, *47*, 4710–4728.

(242) Rajasree, S. S.; Li, X.; Deria, P. Physical properties of porphyrin-based crystalline metal–organic frameworks. *Commun. Chem.* **2021**, *4*, 1–14.

(243) Oleson, A.; Zhu, T.; Dunn, I. S.; Bialas, D.; Bai, Y.; Zhang, W.; Dai, M.; Reichman, D. R.; Tempelaar, R.; Huang, L. et al. Perylene diimide-based hj-and hj-aggregates: The prospect of exciton band shape engineering in organic materials. *J. Phys. Chem. C* **2019**, *123*, 20567–20578.

(244) Kaufmann, C.; Bialas, D.; Stolte, M.; Würthner, F. Discrete π-stacks of perylene bisimide dyes within folda-dimers: insight into long-and short-range exciton coupling. *J. Am. Chem. Soc.* **2018**, *140*, 9986–9995.

(245) Beljonne, D.; Pourtois, G.; Silva, C.; Hennebicq, E.; Herz, L.; Friend, R.; Scholes, G.; Setayesh, S.; Müllen, K.; Brédas, J. Interchain vs. intrachain energy transfer in acceptor-capped conjugated polymers. *Proc. Natl. Acad. Sci.* **2002**, *99*, 10982–10987.

(246) Chang, J. C. Monopole effects on electronic excitation interactions between large molecules. I. Application to energy transfer in chlorophylls. *J. Chem. Phys.* **1977**, *67*, 3901–3909.

(247) Mostofi, A. A.; Yates, J. R.; Lee, Y.-S.; Souza, I.; Vanderbilt, D.; Marzari, N. wannier90: A tool for obtaining maximally-localised Wannier functions. *Comput. Phys. Commun.* **2008**, *178*, 685–699.

(248) Coropceanu, V.; Malagoli, M.; André, J.-M.; Brédas, J.-L. Charge-transfer transitions in triarylamine mixed-valence systems: a joint density functional theory and vibronic coupling study. *J. Am. Chem. Soc.* **2002**, *124*, 10519–10530.

(249) Andrzejak, M.; Petelenz, P. Vibronic relaxation energies of acene-related molecules upon excitation or ionization. *Phys. Chem. Chem. Phys.* **2018**, *20*, 14061–14071.

(250) Qarai, M. B.; Ghosh, R.; Spano, F. C. Understanding Bipolarons in Conjugated Polymers Using a Multiparticle Holstein Approach. *J. Phys. Chem. C* **2021**, *125*, 24487–24497.

(251) Ghosh, R.; Spano, F. C. Excitons and Polarons in Organic Materials. *Acc. Chem. Res.* **2020**, *53*, 2201–2211.

(252) Merrifield, R. Theory of the vibrational structure of molecular exciton states. *J. Chem. Phys.* **1964**, *40*, 445–450.

(253) Meskers, S. C.; Janssen, R. A.; Haverkort, J. E.; Wolter, J. H. Relaxation of photo-excitations in films of oligo-and poly-(para-phenylene vinylene) derivatives. *Chem. Phys.* **2000**, *260*, 415–439.

(254) McRae, E. Molecular vibrations in the exciton theory for molecular aggregates. IV. Excited states of weakly-coupled systems. *Aust. J. Chem.* **1963**, *16*, 295–314.

(255) Bässler, H. Localized states and electronic transport in single component organic solids with diagonal disorder. *Phys. Status Solidi B* **1981**, *107*, 9–54.

(256) Knapp, E. Lineshapes of molecular aggregates, exchange narrowing and intersite correlation. *Chem. Phys.* **1984**, *85*, 73–82.

(257) Bialas, A. L.; Spano, F. C. A Holstein–Peierls Approach to Excimer Spectra: The Evolution from Vibronically Structured to Unstructured Emission. *J. Phys. Chem. C* **2022**, *126*, 4067–4081.

(258) Giaimo, J. M.; Lockard, J. V.; Sinks, L. E.; Scott, A. M.; Wilson, T. M.; Wasielewski, M. R. Excited singlet states of covalently bound, cofacial dimers and trimers of perylene-3, 4: 9, 10-bis (dicarboximide) s. *J. Phys. Chem. A* **2008**, *112*, 2322–2330.

(259) Veldman, D.; Chopin, S. M.; Meskers, S. C.; Groeneveld, M. M.; Williams, R. M.; Janssen, R. A. Triplet formation involving a polar transition state in a well-defined intramolecular perylenediimide dimeric aggregate. *J. Phys. Chem. A* **2008**, *112*, 5846–5857.

(260) Frenkel, J. On the transformation of light into heat in solids. I. *Phys. Rev.* **1931**, *37*, 17.

(261) Frenkel, J. On the transformation of light into heat in solids. II. *Phys. Rev.* **1931**, *37*, 1276.

(262) Kasha, M. Relation between exciton bands and conduction bands in molecular lamellar systems. *Rev. Mod. Phys.* **1959**, *31*, 162.

(263) Kasha, M. Energy transfer mechanisms and the molecular exciton model for molecular aggregates. *Radiat. Res.* **1963**, *20*, 55–70.

(264) Kasha, M.; Rawls, H. R.; El-Bayoumi, M. A. The exciton model in molecular spectroscopy. *Pure and applied Chemistry* **1965**, *11*, 371–392.

(265) McRae, E. G.; Kasha, M. Enhancement of phosphorescence ability upon aggregation of dye molecules. *J. Chem. Phys.* **1958**, *28*, 721–722.

(266) Hochstrasser, R. M.; Kasha, M. Application of the exciton model to mono-molecular lamellar systems. *Photochem. Photobiol.* **1964**, *3*, 317–331.

(267) Keller, N.; Calik, M.; Sharapa, D.; Soni, H. R.; Zehetmaier, P. M.; Rager, S.; Auras, F.; Jakowetz, A. C.; Görling, A.; Clark, T. et al. Enforcing extended porphyrin J-aggregate stacking in covalent organic frameworks. *J. Am. Chem. Soc.* **2018**, *140*, 16544–16552.

(268) Ding, X.; Guo, J.; Feng, X.; Honsho, Y.; Guo, J.; Seki, S.; Maitarad, P.; Saeki, A.; Nagase, S.; Jiang, D. Synthesis of metallophthalocyanine covalent organic frameworks that exhibit high carrier mobility and photoconductivity. *Angew. Chem. Int. Ed.* **2011**, *50*, 1289–1293.

(269) Yin, H.-Q.; Yin, F.; Yin, X.-B. Strong dual emission in covalent organic frameworks induced by ESIPT. *Chem. Sci.* **2019**, *10*, 11103–11109.

(270) Wu, X.; Han, X.; Liu, Y.; Liu, Y.; Cui, Y. Control interlayer stacking and chemical stability of two-dimensional covalent organic frameworks via steric tuning. *J. Am. Chem. Soc.* **2018**, *140*, 16124–16133.

(271) Albacete, P.; Martinez, J. I.; Li, X.; Lopez-Moreno, A.; Mena-Hernando, S.; Platero-Prats, A. E.; Montoro, C.; Loh, K. P.; Perez, E. M.; Zamora, F. Layer-stacking-driven fluorescence in a two-dimensional imine-linked covalent organic framework. *J. Am. Chem. Soc.* **2018**, *140*, 12922–12929.

(272) Fan, Y.; Wen, Q.; Zhan, T.-G.; Qi, Q.-Y.; Xu, J.-Q.; Zhao, X. A case study on the influence of substitutes on interlayer stacking of 2D covalent organic frameworks. *Chem. Eur. J.* **2017**, *23*, 5668–5672.

(273) Kang, C.; Zhang, Z.; Wee, V.; Usadi, A. K.; Calabro, D. C.; Baugh, L. S.; Wang, S.; Wang, Y.; Zhao, D. Interlayer Shifting in Two-Dimensional Covalent Organic Frameworks. *J. Am. Chem. Soc.* **2020**, *142*, 12995–13002.

(274) Ascherl, L.; Sick, T.; Margraf, J. T.; Lapidus, S. H.; Calik, M.; Hettstedt, C.; Karaghiosoff, K.; Döblinger, M.; Clark, T.; Chapman, K. W. et al. Molecular docking sites

designed for the generation of highly crystalline covalent organic frameworks. *Nat. Chem.* **2016**, *8*, 310–316.

(275) Spitler, E. L.; Koo, B. T.; Novotney, J. L.; Colson, J. W.; Uribe-Romo, F. J.; Gutierrez, G. D.; Clancy, P.; Dichtel, W. R. A 2D covalent organic framework with 4.7-nm pores and insight into its interlayer stacking. *J. Am. Chem. Soc.* **2011**, *133*, 19416–19421.

(276) Zhou, W.; Wu, H.; Yildirim, T. Structural stability and elastic properties of prototypical covalent organic frameworks. *Chem. Phys. Lett.* **2010**, *499*, 103–107.

(277) Lukose, B.; Kuc, A.; Heine, T. The structure of layered covalent-organic frameworks. *Chem. Eur. J.* **2011**, *17*, 2388–2392.

(278) Yamagata, H.; Spano, F. C. Interplay between intrachain and interchain interactions in semiconducting polymer assemblies: The HJ-aggregate model. *J. Chem. Phys.* **2012**, *136*, 184901.

(279) Yamagata, H.; Maxwell, D.; Fan, J.; Kittilstved, K.; Briseno, A.; Barnes, M.; Spano, F. HJ-aggregate behavior of crystalline 7, 8, 15, 16-tetraazaterrylene: Introducing a new design paradigm for organic materials. *J. Phys. Chem. C* **2014**, *118*, 28842–28854.

(280) Spano, F. C.; Silva, C. H-and J-aggregate behavior in polymeric semiconductors. *Annu. Rev. Phys. Chem* **2014**, *65*, 477–500.

(281) Gutiérrez-Meza, E.; Malatesta, R.; Li, H.; Bargigia, I.; Srimath Kandada, A. R.; Valverde-Chávez, D. A.; Kim, S.-M.; Li, H.; Stingelin, N.; Tretiak, S. et al. Frenkel biexcitons in hybrid HJ photophysical aggregates. *Sci. Adv.* **2021**, *7*, eabi5197.

(282) Deshmukh, A. P.; Koppel, D.; Chuang, C.; Cadena, D. M.; Cao, J.; Caram, J. R. Design principles for two-dimensional molecular aggregates using Kasha's model: tunable photo-physics in near and short-wave infrared. *J. Phys. Chem. C* **2019**, *123*, 18702–18710.

(283) Jin, X.-H.; Price, M. B.; Finnegan, J. R.; Boott, C. E.; Richter, J. M.; Rao, A.; Menke, S. M.; Friend, R. H.; Whittell, G. R.; Manners, I. Long-range exciton transport in conjugated polymer nanofibers prepared by seeded growth. *Science* **2018**, *360*, 897–900.

(284) Baghgar, M.; Labastide, J. A.; Bokel, F.; Hayward, R. C.; Barnes, M. D. Effect of polymer chain folding on the transition from H-to J-aggregate behavior in P3HT nanofibers. *J. Phys. Chem. C* **2014**, *118*, 2229–2235.

(285) Eder, T.; Vogelsang, J.; Bange, S.; Remmerssen, K.; Schmitz, D.; Jester, S.-S.; Keller, T. J.; Höger, S.; Lupton, J. M. Interplay Between J-and H-Type Coupling in Aggregates of π-Conjugated Polymers: A Single-Molecule Perspective. *Angew. Chem. Int. Ed.* **2019**, *58*, 18898–18902.

(286) Eder, T.; Kraus, D.; Höger, S.; Vogelsang, J.; Lupton, J. M. Vibrations Responsible for Luminescence from HJ-Aggregates of Conjugated Polymers Identified by Cryogenic Spectroscopy of Single Nanoparticles. *ACS nano* **2022**, *16*, 6382–6393.

(287) Balooch Qarai, M.; Chang, X.; Spano, F. Vibronic exciton model for low bandgap donor–acceptor polymers. *J. Chem. Phys.* **2020**, *153*, 244901.

(288) Jin, S.; Supur, M.; Addicoat, M.; Furukawa, K.; Chen, L.; Nakamura, T.; Fukuzumi, S.; Irle, S.; Jiang, D. Creation of superheterojunction polymers via direct polycondensation: segregated and bicontinuous donor–acceptor π-columnar arrays in covalent organic frameworks for long-lived charge separation. *J. Am. Chem. Soc.* **2015**, *137*, 7817–7827.

(289) Mizuguchi, J.; Tojo, K. Electronic structure of perylene pigments as viewed from the crystal structure and excitonic interactions. *J. Phys. Chem. B* **2002**, *106*, 767–772.

(290) Hartnett, P. E.; Timalsina, A.; Matte, H. R.; Zhou, N.; Guo, X.; Zhao, W.; Facchetti, A.; Chang, R. P.; Hersam, M. C.; Wasielewski, M. R. et al. Slip-stacked perylenediimides as an alternative strategy for high efficiency nonfullerene acceptors in organic photovoltaics. *J. Am. Chem. Soc.* **2014**, *136*, 16345–16356.

(291) Eaton, S. W.; Shoer, L. E.; Karlen, S. D.; Dyar, S. M.; Margulies, E. A.; Veldkamp, B. S.; Ramanan, C.; Hartzler, D. A.; Savikhin, S.; Marks, T. J. et al. Singlet exciton fission in polycrystalline thin films of a slip-stacked perylenediimide. *J. Am. Chem. Soc.* **2013**, *135*, 14701–14712.

(292) Yagai, S.; Seki, T.; Karatsu, T.; Kitamura, A.; Würthner, F. Transformation from H-to J-aggregated perylene bisimide dyes by complexation with cyanurates. *Angew. Chem. Int. Ed.* **2008**, *47*, 3367–3371.

(293) Ghosh, S.; Li, X.-Q.; Stepanenko, V.; Würthner, F. Control of H-and J-type π stacking by peripheral alkyl chains and self-sorting phenomena in perylene bisimide homo-and heteroaggregates. *Chem. Eur. J.* **2008**, *14*, 11343–11357.

(294) Sarbu, A.; Biniek, L.; Guenet, J.-M.; Mésini, P. J.; Brinkmann, M. Reversible J-to H-aggregate transformation in thin films of a perylenebisimide organogelator. *J. Mater. Chem. C* **2015**, *3*, 1235–1242.

(295) Bessinger, D.; Ascherl, L.; Auras, F.; Bein, T. Spectrally switchable photodetection with near-infrared-absorbing covalent organic frameworks. *J. Am. Chem. Soc.* **2017**, *139*, 12035–12042.

(296) Bessinger, D.; Muggli, K.; Beetz, M.; Auras, F.; Bein, T. Fast-Switching Vis–IR Electrochromic Covalent Organic Frameworks. *J. Am. Chem. Soc.* **2021**, *143*, 7351–7357.

(297) Li, X.; Gao, Q.; Aneesh, J.; Xu, H.-S.; Chen, Z.; Tang, W.; Liu, C.; Shi, X.; Adarsh, K.; Lu, Y. et al. Molecular engineering of bandgaps in covalent organic frameworks. *Chem. Mater.* **2018**, *30*, 5743–5749.

(298) Wang, M.; Ballabio, M.; Wang, M.; Lin, H.-H.; Biswal, B. P.; Han, X.; Paasch, S.; Brunner, E.; Liu, P.; Chen, M. et al. Unveiling electronic properties in metal–phthalocyanine-based pyrazine-linked conjugated two-dimensional covalent organic frameworks. *J. Am. Chem. Soc.* **2019**, *141*, 16810–16816.

(299) Kim, T. W.; Jun, S.; Ha, Y.; Yadav, R. K.; Kumar, A.; Yoo, C.-Y.; Oh, I.; Lim, H.-K.; Shin, J. W.; Ryoo, R. et al. Ultrafast charge transfer coupled with lattice phonons in two-dimensional covalent organic frameworks. *Nat. Commun.* **2019**, *10*, 1–10.

(300) Tao, W.; Zhang, Y.; Zhu, H. Dynamic Exciton Polaron in Two-Dimensional Lead Halide Perovskites and Implications for Optoelectronic Applications. *Acc. Chem. Res.* **2022**, *55*, 345–353.

(301) Marongiu, D.; Saba, M.; Quochi, F.; Mura, A.; Bongiovanni, G. The role of excitons in 3D and 2D lead halide perovskites. *J. Mater. Chem. C* **2019**, *7*, 12006–12018.

(302) Hjalmarson, H. P.; Büttner, H.; Dow, J. D. Theory of core excitons. *Phy. Rev. B* **1981**, *24*, 6010.

(303) Brazovskii, S.; Kirova, N. Physical theory of excitons in conducting polymers. *Chem. Soc. Rev.* **2010**, *39*, 2453–2465.

(304) Mauck, C. M.; Tisdale, W. A. Excitons in 2D organic–inorganic halide perovskites. *Trends Chem.* **2019**, *1*, 380–393.

(305) Urban, J. M.; Chehade, G.; Dyksik, M.; Menahem, M.; Surrente, A.; Trippé-Allard, G.; Maude, D. K.; Garrot, D.; Yaffe, O.; Deleporte, E. et al. Revealing Excitonic Phonon Coupling in (PEA) 2 (MA) n- 1Pb n I3 n+ 1 2D Layered Perovskites. *J. Phys. Chem. Lett.* **2020**, *11*, 5830–5835.

(306) Straus, D. B.; Iotov, N.; Gau, M. R.; Zhao, Q.; Carroll, P. J.; Kagan, C. R. Longer cations increase energetic disorder in excitonic 2D hybrid perovskites. *J. Phys. Chem. Lett.* **2019**, *10*, 1198–1205.

(307) Thouin, F.; Valverde-Chávez, D. A.; Quarti, C.; Cortecchia, D.; Bargigia, I.; Beljonne, D.; Petrozza, A.; Silva, C.; Srimath Kandada, A. R. Phonon coherences reveal the polaronic

character of excitons in two-dimensional lead halide perovskites. *Nat. Mater.* **2019**, *18*, 349–356.

(308) Zhai, Y.; Baniya, S.; Zhang, C.; Li, J.; Haney, P.; Sheng, C.-X.; Ehrenfreund, E.; Vardeny, Z. V. Giant Rashba splitting in 2D organic-inorganic halide perovskites measured by transient spectroscopies. *Sci. Adv.* **2017**, *3*, e1700704.

(309) Posmyk, K.; Zawadzka, N.; Dyksik, M.; Surrente, A.; Maude, D. K.; Kazimierczuk, T.; Babiński, A.; Molas, M. R.; Paritmongkol, W.; Mączka, M. et al. Quantification of Exciton Fine Structure Splitting in a Two-Dimensional Perovskite Compound. *J. Phys. Chem. Lett.* **2022**, *13*, 4463–4469.

(310) Mitzi, D. B.; Chondroudis, K.; Kagan, C. R. Design, structure, and optical properties of organic- inorganic perovskites containing an oligothiophene chromophore. *Inorg. Chem.* **1999**, *38*, 6246–6256.

(311) Janke, S. M.; Qarai, M. B.; Blum, V.; Spano, F. C. Frenkel–Holstein Hamiltonian applied to absorption spectra of quaterthiophene-based 2D hybrid organic–inorganic perovskites. *J. Chem. Phys.* **2020**, *152*, 144702.

(312) Kataoka, T.; Kondo, T.; Ito, R.; Sasaki, S.; Uchida, K.; Miura, N. Magneto-optical study on excitonic spectra in (C 6 H 13 NH 3) 2 PbI 4. *Phys. Rev. B* **1993**, *47*, 2010.

(313) Baranowski, M.; Zelewski, S. J.; Kepenekian, M.; Traoré, B.; Urban, J. M.; Surrente, A.; Galkowski, K.; Maude, D. K.; Kuc, A.; Booker, E. P. et al. Phase-transition-induced carrier mass enhancement in 2D Ruddlesden–Popper perovskites. *ACS Energy Lett.* **2019**, *4*, 2386–2392.

(314) Gauthron, K.; Lauret, J.; Doyennette, L.; Lanty, G.; Al Choueiry, A.; Zhang, S.; Brehier, A.; Largeau, L.; Mauguin, O.; Bloch, J. et al. Optical spectroscopy of two-dimensional layered (C6H5C2H4-NH3) 2-PbI4 perovskite. *Opt. Express* **2010**, *18*, 5912–5919.

(315) Liang, C.; Cheng, L.; Zhang, S.; Yang, S.; Liu, W.; Xie, J.; Li, M.-D.; Chai, Z.; Wang, Y.; Wang, S. Boosting the Optoelectronic Performance by Regulating Exciton Behaviors in a Porous Semiconductive Metal–Organic Framework. *J. Am. Chem. Soc.* **2022**, *144*, 2189–2196.

(316) Mähringer, A.; Jakowetz, A. C.; Rotter, J. M.; Bohn, B. J.; Stolarczyk, J. K.; Feldmann, J.; Bein, T.; Medina, D. D. Oriented thin films of electroactive triphenylene catecholate-based two-dimensional metal–organic frameworks. *ACS nano* **2019**, *13*, 6711–6719.

(317) Mähringer, A.; Döblinger, M.; Hennemann, M.; Gruber, C.; Fehn, D.; Scheurle, P. I.; Hosseini, P.; Santourian, I.; Schirmacher, A.; Rotter, J. M. et al. An Electrically Conducting Three-Dimensional Iron–Catecholate Porous Framework. *Angew. Chem. Int. Ed.* **2021**, *60*, 18065–18072.

(318) Dou, J.-H.; Arguilla, M. Q.; Luo, Y.; Li, J.; Zhang, W.; Sun, L.; Mancuso, J. L.; Yang, L.; Chen, T.; Parent, L. R. et al. Atomically precise single-crystal structures of electrically conducting 2D metal–organic frameworks. *Nat. Mater.* **2021**, *20*, 222–228.

(319) Northrup, J. E. Atomic and electronic structure of polymer organic semiconductors: P3HT, PQT, and PBTTT. *Phys. Rev. B* **2007**, *76*, 245202.

(320) Spano, F. C.; Yamagata, H. Vibronic coupling in J-aggregates and beyond: a direct means of determining the exciton coherence length from the photoluminescence spectrum. *J. Phys. Chem. B* **2011**, *115*, 5133–5143.

(321) Österbacka, R.; An, C. P.; Jiang, X.; Vardeny, Z. V. Two-dimensional electronic excitations in self-assembled conjugated polymer nanocrystals. *Science* **2000**, *287*, 839–842.

(322) Jiang, X. M.; Österbacka, R.; Korovyanko, O.; An, C. P.; Horovitz, B.; Janssen, R. A.; Vardeny, Z. V. Spectroscopic studies of photoexcitations in regioregular and regiorandom polythiophene films. *Adv. Funct. Mater.* **2002**, *12*, 587–597.

(323) Sirringhaus, H.; Brown, P.; Friend, R.; Nielsen, M. M.; Bechgaard, K.; Langeveld-Voss, B.; Spiering, A.; Janssen, R. A.; Meijer, E.; Herwig, P. et al. Two-dimensional charge transport in self-organized, high-mobility conjugated polymers. *Nature* **1999**, *401*, 685–688.

(324) Chang, J.-F.; Clark, J.; Zhao, N.; Sirringhaus, H.; Breiby, D. W.; Andreasen, J. W.; Nielsen, M. M.; Giles, M.; Heeney, M.; McCulloch, I. Molecular-weight dependence of interchain polaron delocalization and exciton bandwidth in high-mobility conjugated polymers. *Phys. Rev. B* **2006**, *74*, 115318.

(325) Chang, J.-F.; Sirringhaus, H.; Giles, M.; Heeney, M.; McCulloch, I. Relative importance of polaron activation and disorder on charge transport in high-mobility conjugated polymer field-effect transistors. *Phys. Rev. B* **2007**, *76*, 205204.

(326) Brown, P. J.; Thomas, D. S.; Köhler, A.; Wilson, J. S.; Kim, J.-S.; Ramsdale, C. M.; Sirringhaus, H.; Friend, R. H. Effect of interchain interactions on the absorption and emission of poly (3-hexylthiophene). *Phys. Rev. B* **2003**, *67*, 064203.

(327) Kim, N.; Kee, S.; Lee, S. H.; Lee, B. H.; Kahng, Y. H.; Jo, Y.-R.; Kim, B.-J.; Lee, K. Highly conductive PEDOT: PSS nanofibrils induced by solution-processed crystallization. *Adv. Mater.* **2014**, *26*, 2268–2272.

(328) Shirakawa, H. Synthesis and characterization of highly conducting polyacetylene. *Synth. Met.* **1995**, *69*, 3–8.

(329) Skorupskii, G.; Trump, B. A.; Kasel, T. W.; Brown, C. M.; Hendon, C. H.; Dincă, M. Efficient and tunable one-dimensional charge transport in layered lanthanide metal–organic frameworks. *Nat. Chem.* **2020**, *12*, 131–136.

(330) Darago, L. E.; Aubrey, M. L.; Yu, C. J.; Gonzalez, M. I.; Long, J. R. Electronic conductivity, ferrimagnetic ordering, and reductive insertion mediated by organic mixed-valence in a ferric semiquinoid metal–organic framework. *J. Am. Chem. Soc.* **2015**, *137*, 15703–15711.

(331) Calvani, P.; Paolone, A.; Dore, P.; Lupi, S.; Maselli, P.; Medaglia, P.; Cheong, S.-W. Infrared response of ordered polarons in layered perovskites. *Phys. Rev. B* **1996**, *54*, R9592.

(332) Scholes, D. T.; Yee, P. Y.; Lindemuth, J. R.; Kang, H.; Onorato, J.; Ghosh, R.; Luscombe, C. K.; Spano, F. C.; Tolbert, S. H.; Schwartz, B. J. The Effects of Crystallinity on Charge Transport and the Structure of Sequentially Processed F4TCNQ-Doped Conjugated Polymer Films. *Adv. Funct. Mater.* **2017**, *27*, 1702654.

(333) Aubry, T. J.; Axtell, J. C.; Basile, V. M.; Winchell, K.; Lindemuth, J. R.; Porter, T. M.; Liu, J.-Y.; Alexandrova, A. N.; Kubiak, C. P.; Tolbert, S. H. et al. Dodecaborane-Based Dopants Designed to Shield Anion Electrostatics Lead to Increased Carrier Mobility in a Doped Conjugated Polymer. *Adv. Mater.* **2019**, *31*, 1805647.

(334) Kahmann, S.; Loi, M. A.; Brabec, C. J. Delocalisation softens polaron electronic transitions and vibrational modes in conjugated polymers. *J. Mater. Chem. C* **2018**, *6*, 6008–6013.

(335) Zhong, Y.; Untilova, V.; Muller, D.; Guchait, S.; Kiefer, C.; Herrmann, L.; Zimmermann, N.; Brosset, M.; Heiser, T.; Brinkmann, M. Preferential Location of Dopants in the Amorphous Phase of Oriented Regioregular Poly (3-hexylthiophene-2, 5-diyl) Films Helps Reach Charge Conductivities of 3000 S cm- 1. *Adv. Funct. Mater.* **2022**, 2202075.

(336) Thomas, E. M.; Peterson, K. A.; Balzer, A. H.; Rawlings, D.; Stingelin, N.; Segalman, R. A.; Chabinyc, M. L. Effects of Counter-Ion Size on Delocalization of Carriers and Stability of Doped Semiconducting Polymers. *Adv. Electron. Mater.* **2020**, *6*, 2000595.

(337) Jin, S.; Sakurai, T.; Kowalczyk, T.; Dalapati, S.; Xu, F.; Wei, H.; Chen, X.; Gao, J.; Seki, S.; Irle, S. et al. Two-dimensional tetrathiafulvalene covalent organic frameworks: towards latticed conductive organic salts. *Chem. Eur. J.* **2014**, *20*, 14608–14613.

(338) Li, X.; Qiao, J.; Chee, S. W.; Xu, H.-S.; Zhao, X.; Choi, H. S.; Yu, W.; Quek, S. Y.; Mirsaidov, U.; Loh, K. P. Rapid, Scalable Construction of Highly Crystalline Acylhydrazone

Two-dimensional Covalent Organic Frameworks via Dipole-Induced Antiparallel Stacking. *J. Am. Chem. Soc.* **2020**, *142*, 4932–4943.

(339) Pütz, A. M.; Terban, M. W.; Bette, S.; Haase, F.; Dinnebier, R. E.; Lotsch, B. V. Total scattering reveals the hidden stacking disorder in a 2D covalent organic framework. *Chem. Sci.* **2020**, *11*, 12647–12654.

(340) Auras, F.; Ascherl, L.; Hakimioun, A. H.; Margraf, J. T.; Hanusch, F. C.; Reuter, S.; Bessinger, D.; Döblinger, M.; Hettstedt, C.; Karaghiosoff, K. et al. Synchronized offset stacking: a concept for growing large-domain and highly crystalline 2D covalent organic frameworks. *J. Am. Chem. Soc.* **2016**, *138*, 16703–16710.

(341) Kuc, A.; Springer, M. A.; Batra, K.; Juarez-Mosqueda, R.; Wöll, C.; Heine, T. Proximity Effect in Crystalline Framework Materials: Stacking-Induced Functionality in MOFs and COFs. *Adv. Func. Mater.* **2020**, *30*, 1908004.

(342) Liu, C.-H.; Wei, A.; Cheung, M. F.; Perepichka, D. F. Vanishing Electronic Band Gap in Two-Dimensional Hydrogen-Bonded Organic Frameworks. *Chem. Mater.* **2022**, *34*, 3461–3467.

(343) Medina, D. D.; Petrus, M. L.; Jumabekov, A. N.; Margraf, J. T.; Weinberger, S.; Rotter, J. M.; Clark, T.; Bein, T. Directional charge-carrier transport in oriented benzodithiophene covalent organic framework thin films. *ACS Nano* **2017**, *11*, 2706–2713.

(344) Doheny, P. W.; Clegg, J. K.; Tuna, F.; Collison, D.; Kepert, C. J.; D'Alessandro, D. M. Quantification of the mixed-valence and intervalence charge transfer properties of a cofacial metal–organic framework via single crystal electronic absorption spectroscopy. *Chem. Sci.* **2020**, *11*, 5213–5220.

(345) Ding, B.; Hua, C.; Kepert, C. J.; D'Alessandro, D. M. Influence of structure–activity relationships on through-space intervalence charge transfer in metal–organic frameworks with cofacial redox-active units. *Chem. Sci.* **2019**, *10*, 1392–1400.

(346) Aubrey, M. L.; Wiers, B. M.; Andrews, S. C.; Sakurai, T.; Reyes-Lillo, S. E.; Hamed, S. M.; Yu, C.-J.; Darago, L. E.; Mason, J. A.; Baeg, J.-O. et al. Electron delocalization and charge mobility as a function of reduction in a metal–organic framework. *Nat. Mater.* **2018**, *17*, 625–632.

(347) Yoshizawa, M.; Kumazawa, K.; Fujita, M. Room-temperature and solution-state observation of the mixed-valence cation radical dimer of tetrathiafulvalene,[(TTF) 2]+•, within a self-assembled cage. *J. Am. Chem. Soc.* **2005**, *127*, 13456–13457.

(348) Capizzi, M.; Calvani, P.; Dore, P.; Lupi, S.; Maselli, P.; Paolone, A.; Ruzicka, B.; Sadowski, W.; Cheong, S.-W. Weakly and tightly bound polarons in the infrared spectra of perovskites. *Phys. Scr.* **1996**, *1996*, 215.

(349) Wong, W. P.; Yin, J.; Chaudhary, B.; Chin, X. Y.; Cortecchia, D.; Lo, S.-Z. A.; Grimsdale, A. C.; Mohammed, O. F.; Lanzani, G.; Soci, C. Large polaron self-trapped states in three-dimensional metal-halide perovskites. *ACS Mater. Lett.* **2019**, *2*, 20–27.

(350) Moulé, A. J.; Gonel, G.; Murrey, T. L.; Ghosh, R.; Saska, J.; Shevchenko, N. E.; Denti, I.; Fergerson, A. S.; Talbot, R. M.; Yacoub, N. L. et al. Quantifying Polaron Mole Fractions and Interpreting Spectral Changes in Molecularly Doped Conjugated Polymers. *Adv. Electron. Mater.* **2022**, *8*, 2100888.

(351) Hernandez, V.; Roman, J. E.; Vidal, V. SLEPc: A scalable and flexible toolkit for the solution of eigenvalue problems. *ACM Trans. Math. Software* **2005**, *31*, 351–362.

(352) Roman, J. E.; Campos, C.; Romero, E.; Tomas, A. *SLEPc Users Manual*; 2020.

(353) Balay, S.; Abhyankar, S.; Adams, M. F.; Brown, J.; Brune, P.; Buschelman, K.; Dalcin, L.; Dener, A.; Eijkhout, V.; Gropp, W. D. et al. PETSc Web page. `https://www.mcs.anl.gov/petsc`, 2019; `https://www.mcs.anl.gov/petsc`.